Masked stereolithography of hydroxyapatite bioceramic scaffolds

Pedro Navarrete-Segado, Mallorie Tourbin, Christine Frances, David Grossin

Open Ceramics 9 (2022) 100235

Contents lists available at ScienceDirect

Open Ceramics

journal homepage: www.sciencedirect.com/journal/open-ceramics

Masked stereolithography of hydroxyapatite bioceramic scaffolds: From powder tailoring to evaluation of 3D printed parts properties

Pedro Navarrete-Segado [a,b], Mallorie Tourbin [b], Christine Frances [b], David Grossin [a,*]

[a] CIRIMAT, Université de Toulouse, CNRS, 4 Allée Émile Monso, 31030, Toulouse Cedex 4, France
[b] Laboratoire de Génie Chimique, Université de Toulouse, CNRS, 4 Allée Émile Monso, 31432, Toulouse Cedex 4, France

ARTICLE INFO

Keywords:
Hydroxyapatite
Rheology
Sedimentation
Suspensions
Mechanical properties
VAT photopolymerization
Additive manufacturing

ABSTRACT

This paper focuses on the tailoring of hydroxyapatite powders properties for the preparation of highly hydroxyapatite-loaded photocurable organic slurries. The suspensions were evaluated as feedstock for the production of hydroxyapatite scaffolds by stereolithography-based additive manufacturing technique. Then, a debinding-sintering process was designed to avoid the formation of cracks during the pyrolysis of the resin and sintering of the printed parts. A total porosity of 35 vol % and compression strength of 4.9 ± 0.3 MPa were obtained for the specimens printed at 45° to the building platform. A slow degradation rate was observed due to the high degree of crystallinity and intrinsic stability of the hydroxyapatite phase. The tailoring of hydroxyapatite powders was required to lower the viscosity and increase the particle stability of the suspensions. The printed hydroxyapatite scaffolds showed promising results for surgery, in the case of minor or non-load bearing implants requiring slow resorption properties.

1. Introduction

People are living longer than ever before with the median age projected to increase by 4.5 years between 2019 and 2050 [1]. This ageing increase leads to a growth of incidence of bone injuries and deficiencies [2]. In the last decades, the rising interest for new efficient therapies has brought wide progress on the use of biomaterials such as calcium phosphate-based bioceramics [3]. Reparation of fractured or diseased bone needs to start from a scaffold or three-dimensional (3D) construct providing the necessary support for the attachment, growth, and proliferation of bone cells [4]. Hydroxyapatite (HA) is one of the most commonly used calcium phosphates bioceramic phases for bone tissue engineering in orthopaedic and dental communities for its excellent biocompatibility, slow degradation, and osteointegration [5]. HA can withstand resorption during healing providing a good scaffold for natural bone growth, their slow resorption properties could be an advantage in maintaining the volumetric stability of the augmented bone. The presence of hard tissue around a dental implant is crucial for the long-term success of implant placement in surgical techniques such as guided bone regeneration and autogenous bone blocks transfer for dental implant placement [6–8]. For block grafts used in regeneration, an ideal biomaterial should meet at least the following characteristics: (i) biocompatibility and controlled biodegradability with sufficient durability to carry out the task for which it was developed [9], (ii) a porous and interconnected design enabling osteoblasts (15–50 μm) and stem cells (5–12 μm) migration, proliferation, and flow transport of nutrients and metabolic waste through the pores [10] (ideal size of the micropores should be at least 400 μm) [11], (iii) mechanical properties matching those of the target tissue at the site of implantation [12], (iv) suitable surface chemistry for cell anchorage, promotion and differentiation [12].

Additive manufacturing (AM) technologies have emerged as an excellent method to fabricate parts suitable for their use in bone tissue engineering applications [13]. They allow the production of allograft custom blocks with defined and reproducible internal structures [14]. Depending on the AM technique, the process basis, methodology, and primary feedstock properties can vary widely [15,16]. Techniques included in the VAT photopolymerization category uses a laser or UV-light source to cross-link a photocurable resin feedstock (composed of a photoinitiator, monomers, or oligomers, reactive diluents, and various additives such as bioceramic powders) [17].

Masked stereolithography (MSLA), also called LCD technique, is the last of these technologies arriving on the market and it has substantially grown in the last years [18]. It uses a direct and perpendicular UV light projection from an array of LEDs and an LCD device acting as a mask to

* Corresponding author.
E-mail address: david.grossin@ensiacet.fr (D. Grossin).

https://doi.org/10.1016/j.oceram.2022.100235
Received 14 January 2022; Accepted 14 February 2022
Available online 19 February 2022

Abbreviation list

3D = Three-dimensional
AM = Additive manufacturing
BET = Brunauer-Emmett-Teller
BJH = Barrett-Joyner-Halenda
BS = Backscattering
CAD = Computer aided design
CaO = Calcium oxide
CT = X-ray computed tomography
FTIR = Fourier-transform infrared
HA = Hydroxyapatite
ICP/AES = Inductively coupled plasma atomic emission spectroscopy
IPA = Isopropyl alcohol
ISO = International Organization for Standardization
LCD = Liquid-crystal display
LED = Light-emitting diode
MSLA = Masked stereolithography
PBM = Planetary ball mill
PEG200 = Polyethylene glycol 200
PSD = Particle size distribution
SBM = Stirred bead mill
SEM = Scanning electron microscopy
TGA = Thermogravimetric analysis
TRIS = Tris(hidroximetil)aminometano
TSI = Turbiscan stability index
TTCP = Tetracalcium phosphate
UV = Ultraviolet
XRD = X-ray diffraction
α-TCP = α-Tricalcium phosphate
β-TCP = β-Tricalcium phosphate

Symbols
x_{10} = the 10th percentile [μm] (diameter of a sphere at which 10% of the particles in the sample are smaller)
x_{50} = Median particle size [μm] = the 50th percentile (diameter of a sphere at which 50% of the particles in the sample are smaller)
x_{90} = The 90th percentile [μm] (diameter of a sphere at which 90% of the particles in the sample are smaller)

selectively polymerize the photocurable feedstock. Some advantages of this LCD technique are the low cost compared with other technologies (laser SLA, DLP …) and the good resolution, although they have a shorter service life and need to be replaced regularly [19]. This and similar techniques have been recently employed for the production of calcium phosphates-based parts [17,20,21]. However, still, some research is needed on the intrinsic relationship between ceramic powder characteristics, solid loading, and dispersion behaviour on the ceramic-loaded photocurable slurry properties [22]. Dispersed powder feedstock inducing a low increase of viscosity, keeping the stability of the suspensions, and showing a good sintering behaviour are pursued since these are crucial properties for a correct performance during the printing process as well as during post-treatments [23–25]. The maximum viscosity for a slurry intended for VAT photopolymerization is approximately 5 Pa s at a low shear rate depending on the printer design [26]. Then, certain stability of the suspensions should be reached avoiding the sedimentation of the particles, which could block the LCD screen and UV light during the printing process [23]. It is also important to use particles which size allows the subsequent debinding-sintering process preventing the formation of cracks. More often, this is achieved by calcium phosphate particles within the micron range (1–20 μm) [27]. This can be reached by modifying the powder particle size distribution through different processes (e.g., milling, sieving …).

Thus, the objective of the present study is to evaluate the effect of the HA-tailored powders with different characteristics on the properties of the highly HA-loaded photocurable slurries. First, the powder showing the most outstanding performance in terms of slurry viscosity (<5 Pa s at a low shear rate (1 s^{-1})), and dispersion stability (Turbiscan stability index <2) during the whole process will be found through comparison. Then, the processability of the suspension will be tested with the printing of HA parts with controlled macroporosity (pore size >400 μm). Finally, the mechanical properties and the dissolution rate of the scaffolds will be determined to assess the HA bioceramic scaffolds efficacy as a bone substitute.

2. Material and methods

2.1. Materials

2.1.1. Stoichiometric hydroxyapatite powders

Stoichiometric hydroxyapatite powder (HA, $Ca_{10}(PO_4)_6(OH)_2$) was used as filler for the suspensions prepared in the present work. The initial powder was produced by Urodelia (SA Company, Saint-Lys, France) via a wet precipitation process (product reference 206.93.003). A deeper explanation of the production of this powder through wet-chemical precipitation was offered in a previous work [28].

HA-filled organic slurries for the MSLA process were produced with three kinds of HA powders (two of them produced by different milling processes) for suspension properties comparison (e.g., stability, rheology …):

- $HA_{Initial}$ powder: the starting HA powder was used as received.
- HA_{PBM} powder: A second powder was crushed through the planetary ball milling (PBM) process of $HA_{Initial}$. A Retsch® planetary-ball mill S 1000 was used to reduce the size of the largest agglomerates present in $HA_{Initial}$ powder. A previously weighted amount of powder (140 g) is poured inside of the 250 ml alumina grinding jar with lid together with the following alumina grinding balls (bulk density: 3600 kg/m^3, mass: 346 g): 3 balls of 30 mm + 12 balls of 20 mm + 9 balls of 10 mm. Then, a ball filling degree of 0.38 (to total chamber volume) and powder filling degree of 0.44 (to ball-filled chamber volume) were used. After 1 h of the milling process at 500 rpm, the HA_{PBM} powder was recovered.
- HA_{SBM} powder: Stirred bead milling process (SBM) was performed in a commercial equipment Labstar manufactured by NETZSCH (Germany) to reduce the size of the HA particles present in $HA_{Initial}$ powder. The detailed scheme of this SBM Labstar equipment and the experimental procedure were already detailed in previous works [29,30]. A water volume was added to the dispersing tank followed by the gradual addition of the weighted HA powder amount to have a final suspension batch of 2 kg with a 10 wt% of solid concentration. It was stirred for 10 min at 600 rpm at 25 °C before starting the pumping and comminution in the milling chamber. Yttrium Stabilized Zirconia 95% (YSZ, ZrO_2) micro grinding beads (Zirmil® Y from WAB-Group) were used for the milling in a 85% of the chamber filling degree (total volume chamber 0.48 l). The nominal size of the beads was 0.35–0.45 mm (laser diffraction particle analysed values x_{10} = 0.32 ± 0.00 mm, x_{50} = 0.39 ± 0.00 mm, and x_{90} = 0.45 ± 0.00, refractive and absorption indices of 2.148 and 1.000) with a density of 6020 kg m^{-3} (bulk density: 3700 kg.m^{-3}). The operational conditions were a stirrer speed of 7.7 m.s^{-1} (2000 rpm), a constant product flow rate of 8.8×10^{-6} m^3 s^{-1}, and specific energy of 720 kJ

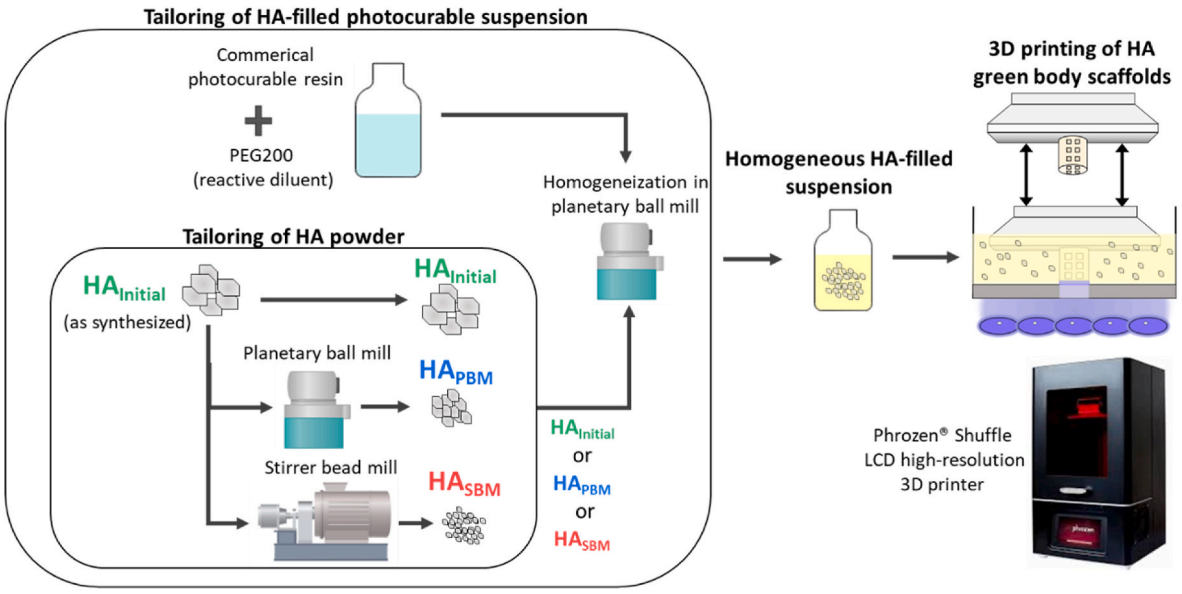

Fig. 1. HA-filled photocurable slurry preparation process.

kg^{-1} (it was equivalent to 60 min of the process). From now on, we will refer to this ground powder as HA_{SBM}. After this wet grinding process, the HA_{SBM} powder had to be vacuum filtered, washed, and dried at 70 °C overnight before its utilization as filler.

2.1.2. Photocurable resin components

The commercial photoreactive resin Dentifix-3D, Modelling HR (high reactive) transparent (clear), from FunToDo® was used as a monomeric and photoinitiator base for the preparation of the organic suspensions. The exact composition of the resin is proprietary information; however, we could describe it as a mixture of approximately 50:50:1 in weight of acrylate monomers, glycol diacrylate monomers, and phosphine oxide base photoinitiator. To improve the rheological behaviour of the suspensions the addition of a reactive diluent was considered. Polyethylene glycol 200 (PEG200) was tested as a diluent and after a heuristic research process, it was found that the maximum amount that could be added without compromising the resin reactivity and performance was 25 vol %. This volume proportion 3:1 of resin base:diluent was kept constant for all the slurries prepared during the study.

2.1.3. Preparation of HA-filled photocurable suspensions

A series of HA-filled photocurable suspensions were prepared to contain different types ($HA_{Initial}$, HA_{PBM}, HA_{SBM}) and concentrations of HA powders for comparison. The preparation consisted of the mixing/homogenization between the HA powder and the organic resin via the PBM process (same equipment used for the preparation of HA_{PBM}). It started with the addition of a previously weighted amount of HA powder (depending on the final concentration) into the grinding jar already containing the same proportion of grinding balls mentioned in the preparation of HA_{PBM}. Then, after pouring the organic resin (mass: 50 g, already containing PEG200) the jar was closed with the lid and stirred by the PBM process at about 500 rpm for 30 min. Just after finishing the process, the resulting HA-filled suspensions were collected for rheology and dispersion stability evaluation and its utilization in an MSLA apparatus. A general view of the HA-filled photocurable slurry preparation is illustrated in Fig. 1.

2.2. Production of HA scaffolds

2.2.1. 3D printing of HA scaffolds via masked stereolithography

Three-dimensional bioceramic green bodies (HA/organic resin composite) were printed by intermittent and selective cross-linking of HA-filled suspension layers. A commercial MSLA equipment, Phrozen® Shuffle, LCD high-resolution 3D-printer was used [31]. It uses an LCD screen with a 5.5-inch 2K resolution reaching an XY resolution of 47 μm. A ParaLED matrix 1.0 optical engine is used as a UV light source with a 90% optical uniformity (better than conventional COB LED). The produced UV light has a wavelength of 405 nm and a power of 50 W.

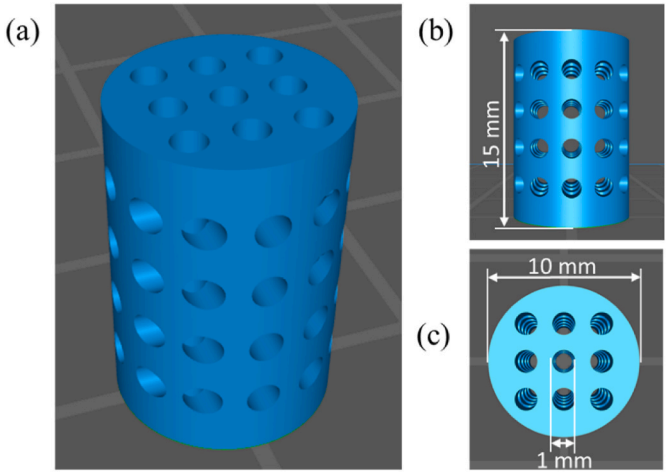

Fig. 2. 3D model used to print the HA parts: (a) perspective, (b) front view, (c) top view.

The process started by loading the previously designed 3D model (Fig. 2) into the printer software. Since compression strength analyses were planned for the samples, the 3D model was designed according to the requirements described in the standard ISO 13175-3:2012 for the tests. The scaffolds model design consisted of a cylinder with 10 mm of diameter and 15 mm of height, with controlled internal and interconnected macro-porosity having circular overtures of 1000 μm in all three directions. Open-source FreeCAD and Chitubox basic software were employed for the design, creation of supports, placement of the models, and slicing. The resin profile was settled by fixing the printing parameters, which are described in Table 1. Basic information refers to the parameters followed during the whole process such as layer thickness, stage down speed, and lighting delay. Then, there is a distinction in

Table 1
MSLA printing parameters profile used for the production of HA scaffolds.

	Basic information			Burn layer (first 6 layers)				Normal layer		
Parameter	Layer height (mm)	Down speed (mm/min)	Delay (ms)	Layers (number)	Cure time (ms)	Lift height (mm)	Up speed (mm/min)	Cure time (ms)	Lift height (mm)	Up speed (mm/min)
Value	0.10	150	1000	6	40000	8	100	10000	7	100

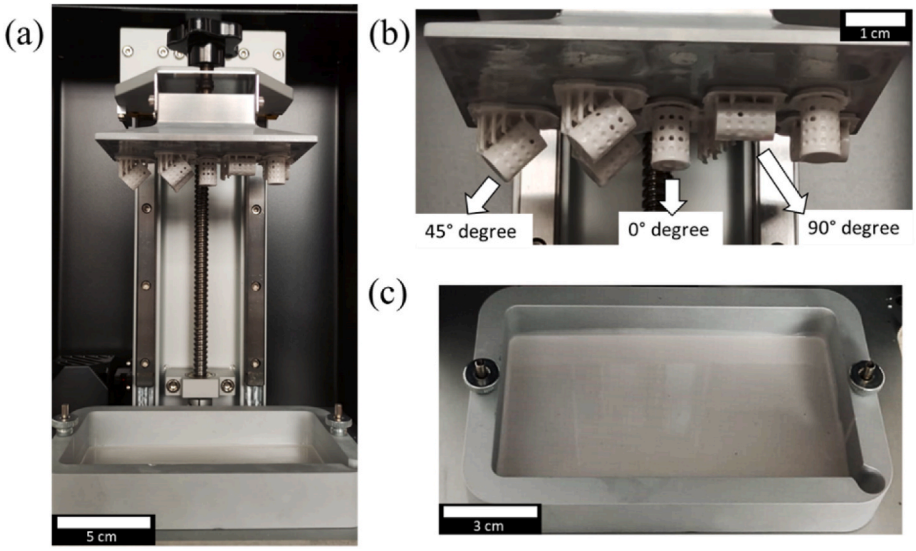

Fig. 3. (a) General view of the MSLA process, (b) printing platform with HA scaffolds with three different printing orientations, and (c) HA-filled slurry container.

the table between the printing parameters (cure time, stage lift height, and up speed) for the first 6 layers (burn layers) and the rest of the layers (normal layers). The same parameters profile was used for the printing of the scaffolds during the study.

Once the printing platform has been calibrated in the z-axis, the slurry is poured inside of the tank container, and with the help of a plastic spatula, it is homogeneously spread to completely cover the FEP film, which separates the resin from the LCD screen. Then the printing process started constructing the model layer by layer combining the curing of the resin by UV light exposition and the movement of the platform in z-axis following the parameters defined. Fig. 3 shows the MSLA process together with the resulting HA bioceramic scaffolds and the tank containing the HA-filled resin. Three different HA scaffold models were designed and printed varying the orientation. Three rotation degrees 0°, 45°, and 90° were applied to the models to study their influence on the quality of the printed parts. All models included supports and rafts to avoid the direct contact of the scaffolds with the printing platform surface.

One time the printing process finished, each raft supporting the scaffold was detached from the platform surface and the supports were carefully cut with tweezers freeing the HA green body scaffold. Then, the scaffolds were soaked in an ultrasonic bath with isopropyl alcohol (IPA) for 3 min. Finally, they were swirled around in the IPA to rinse off the extra uncured resin.

2.2.2. *Debinding-sintering process*

To obtain HA bioceramic scaffolds free of polymer it was necessary to design a one-step debinding-sintering process for the pyrolysis of the cured resin of the printed HA green bodies. Thus, producing in the same process the sintering of the HA particles keeping or improving the mechanical properties of the parts. To prepare the debinding-sintering process, the samples were placed in alumina crucibles and introduced in a muffle furnace Nabertherm® LT 9/13. They were located in a middle height and leaving the same space between the lateral walls inside of the muffle chamber to optimize the heat distribution. The

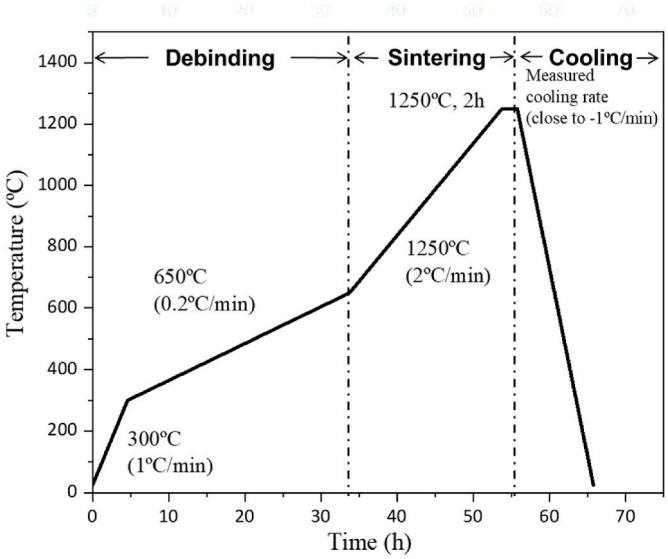

Fig. 4. Programmed temperature pattern for the debinding-sintering process of HA scaffolds.

process was carried out in the air and three different temperature phases (or heating ramps) could be distinguished. First, one heating ramp of 1 °C/min until 300 °C followed by another one of 0.2 °C/min until 650 °C performed the debinding phase. Then the heating was speeded up at 2 °C/min until 1250 °C and kept constant for 2 h to achieve correct sintering of the HA particles. Finally, the furnace was inertially cooled down with an average speed of -1 °C/min to prevent the apparition of cracks due to thermal shocks. The complete temperature pattern followed is described in Fig. 4.

2.3. Characterization techniques

2.3.1. Particle size distribution, porosity, and surface area

A Mastersizer MS 3000 (Malvern Panalytical®) laser particle size analyser (refractive indexes: 1.63 and 1.33 for particles and water, respectively) was used to analyse the PSD of the HA powders by laser diffraction in suspension. It was not possible to analyse the PSD of the HA powders suspended in the photocurable resin due to a risk of polymerization by the blue light (wavelength: 470 nm) used for the measurement. Instead, to simulate their dispersion state they were analysed in aqueous suspension. Ultrapure water used as dispersion medium was produced by the equipment "Purelab Ultra" of VWS (UK) Ltd. Physisorption analysis of powders was quantified in a Micromeritics® TriStar II Plus 3.00 equipment. Samples were previously degassed at 40 °C overnight in a VacPrep™ 061. The data from BJH pore size distribution desorption was used to determine exactly the average pore volume. Nitrogen adsorption-desorption isotherm properties were used to calculate the specific surface area through the BET method.

2.3.2. Turbidimetry analysis

Turbiscan stability index (TSI) (a Turbiscan specific parameter for stability comparison) and backscattered (BS) profiles of the different HA-filled slurries were obtained using a Turbiscan LAB™ (Formulaction®). The light source scanned the sample tube at 2 min intervals from top to bottom and measured the percentage of light BS or transmitted during a 3 h period at 25 °C to cover the total time needed for the printing process of the green bodies (about 2 h). Longer analyses (up to 66 h) were performed to evaluate the time of destabilization. The analysis of the stability was performed as a variation of BS profiles as a function of time at the totality of the sample height. The curves obtained allow a better quantification of their dispersion stability and identify the phenomena taking place in the samples (sedimentation, flocculation …). The overall stability of slurries was examined using the TSI parameters calculated by the Turbiscan software using the formulae below [32]:

$$BS = \frac{1}{\sqrt{\lambda^*}} \tag{1}$$

$$\lambda^*(\varphi, x_{50}) = \frac{2x_{50}}{3\varphi(1-g)Qs} \tag{2}$$

$$TSI = \sqrt{\frac{\sum_{i=1}^{n}(\chi i - \chi BS)^2}{n-1}} \tag{3}$$

where λ^* is the photon transport mean free path in the sample, φ is the volume fraction of particles, x_{50} is the mean diameter of particles, g and Qs are optical parameters given by the Mie theory. χi is the average backscattering for each minute of measurement, χBS is the average χi, and n is the number of scans.

2.3.3. Rheological analysis of suspensions

The rheological behaviour of the organic resin and HA-filled suspensions at different concentrations was examined using a TA Instruments AR2000 rheometer. A 40 mm crosshatched parallel plates system was used as geometry (gap = 1300 μm). Flow curves of each sample were produced at a constant plate temperature of 25 °C controlled by a Peltier plate. An increasing shear rate (steady-step flow step) in the range of 1–100 s^{-1} was used taking ten points by decade.

2.3.4. Chemical and structural analyses

The calcium phosphate crystalline phases in the sintered scaffolds were detected by X-ray diffraction (XRD) analysis at different temperatures by using a BRUKER's X-ray diffractometer D8 Advance system with Cu Kα radiation (wavelength λ = 0.15406 nm). Equipped with a high-temperature sample stage, a LYNXEYE XE-T detector (energy resolution of 0.38 keV) and a nickel filter at 40 kV and 40 mA. Samples were analysed in a 2θ range between 20° and 60°, a step of 0.03° 2θ and a time per step of 0.2 s. Measurements were performed at key temperature values of the temperature pattern used for the debinding-sintering process.

Sintered HA scaffold pieces obtained after the uniaxial compression test were hand-crushed using a mortar and pestle to produce a homogeneous powder. Powdered samples were examined by Fourier transform infrared spectroscopy (FTIR) analysis in a spectrometer FTIR iS50 using the KBr pellet preparation method to determine its chemical composition. Approximately 9 mg of sample powder are transferred to a clean mortar, then a weighed amount of dry KBr powder (300 ± 5 mg) is added and mixed gently to produce a homogenous mixture, followed by compression at 6000 kg for the sample disk preparation. FTIR spectra were recorded in the 4000-400 cm^{-1} wavenumber range with a step width of 0,48 cm^{-1} for each sample disk.

2.3.5. Analysis of macro-structural properties of HA scaffolds

The morphology of HA powders, scaffolds surface, and the cross-section were examined with a scanning electron microscope (SEM) LEO 435 VP (Leica®) equipped with a Ge detector (Imix-PC, Princeton gamma-tech) and a metallization of the ceramic surface was applied with a thin film of silver employing a Scancoat Six sputter coater. HA scaffolds surface was polished in the X, Y plane to analyse the cross-section of the parts. Firstly, the samples were coarse, medium, and fine ground using a Minitech 263 and silicon carbide papers of different grit sizes to reach the region of interest (about 3 mm depth in the X, Y plane). Then, a DiaPro alcohol-based 3 μm high concentration diamond suspension from Struers® and a cloth paper were used in a Struers® Tegrapol 25 to obtain a better surface finishing. ImageJ was used for the processing of the images [33].

High-resolution X-ray micro-computed tomography (CT) analyses of the printed parts were performed in a Nanotom® 180 Phoenix - GE equipped with a 180 kV/15 W high-power nanofocus X-ray tube (9 μm voxel size, resolution). This analysis allowed us to have a 3D perspective of the scaffold and evaluate their total porosity (microstructural porosity of sintered HA and lattice porosity of the scaffold architecture). The data sets were reconstructed and three-dimensionally visualized using VGStudio MAX 4.4 software.

The geometrical density of the scaffolds was calculated from the mass and dimensions of at least ten samples. The theoretical density of HA (3.16 g cm^{-3}) was used as a reference to calculate the total volume fraction of porosity. The open porosity of the scaffolds was measured by Archimedes' method using distilled water as liquid.

The shrinkage of the scaffolds after the debinding-sintering process was studied by comparison of the scaffold's dimensions before and after the thermal treatment. Three measurements of the height at different rotation angles (every 60°) were used to calculate the height average and the z-axis shrinkage of each printed part. For the diameter average and the x, y axes shrinkage, nine measurements were carried out (three measurements at three different heights of the part: bottom, middle, top) also at different rotation angles (every 60°).

Mercury intrusion porosimetry was used to analyse the total connected porosity, volume of pores, and pore size distribution >50 nm (meso- and macropores) of the printed scaffolds. These analyses were performed in an AutoPore IV 9500.

2.3.6. Mechanical properties

The compressive strength of the sintered HA scaffolds with different orientations was measured in a universal mechanical testing press HOUNSFIELD H25KS (Tinius Olsen®, USA). A stainless-steel compression miniature load cell T22-252 U4000 with a range of 25 kN was used to measure the shear force at a crosshead speed of 0.10 mm/min at room temperature. At least ten samples (N = 10) from the same batch were evaluated to calculate the mean values and the standard deviation. The procedure followed is described in the standard ISO-13175:2012. To measure the maximum compressive load taken by the specimens, the

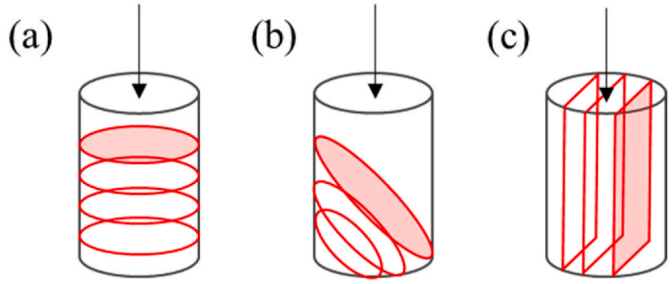

Fig. 5. Direction of loading (black arrows) to printing orientation in compressive testing. (a) 0°, (b) 45°, and (c) 90°.

load given by the testing press in the direction shown in Fig. 5, was increased till the complete failure of the specimens due to crack propagation.

2.3.7. Dissolution rate and pH change

In vitro dissolution rate of the sintered scaffolds, Ca^{2+} ion release, and pH change of the dissolution medium were evaluated following the procedure also described in the standard ISO-13175:2012. Three samples of HA scaffold (printed at orientation 0°) were introduced in three flasks of 0.05 M TRIS buffer solution after nitric acid addition for pH adjustment at 7.3 ± 0.1 at 37 ± 1 °C. The three solution flasks were placed on a plate agitator with a rotation speed of 200 rpm for 24 h, 48 h, and 72 h respectively. The ratio of initial material mass to total dissolution media volume was kept constant at 4.0 mg ml^{-1} pH was measured after 0 h, 24 h, 48 h, and 72 h of immersion. Thus, ensuring that the initial pH value did not vary more than 0.3 during the testing. The Ca^{2+} ion content of the solutions was analysed by ICP/AES in an inductively coupled plasma atomic emission spectrometry (ICP/AES, Ultima2R HORIBA®). The concentrations versus time curves were determined. The test was repeated three times (N = 3) to calculate the mean values and the standard deviation.

2.3.8. Thermal analysis

Thermogravimetric (TGA) and differential scanning calorimetry (DSC) analyses were performed to study and confirm the mass loss evolution of the products and the energy transferred to or from the sample during the debinding-sintering process. It was performed by introducing a small portion (0.02 g) of the ceramic green body in a Setsys Evolution TG92 (Setaram®) and applying a heating ramp of 10 °C/min until 1250 °C in air.

3. Results and discussion

3.1. HA-filled suspension preparation

This section involves the analysis of the three different HA powders ($HA_{Initial}$, HA_{PBM}, HA_{SBM}) properties and the evaluation of their influence on the final HA-filled suspension stability and rheological behaviour. Only the HA-filled suspension showing the best attributes for its application in an MSLA printer will be finally used for the preparation of the HA scaffolds.

3.1.1. HA powders properties comparison

Particle size distribution (PSD) and scanning electron microscopy (SEM) micrographs of each of the three HA powders ($HA_{Initial}$, HA_{PBM}, HA_{SBM}) used for the preparation of the photocurable organic suspensions in the present study are shown in Fig. 6. Clear differences in the particle median sizes (x_{50}) and spans can be observed between the three powders. $HA_{Initial}$ is composed of mainly one population composed of agglomerates produced by the calcination of the powder with an x_{50} of 25 μm.

The use of specific milling conditions during the SBM process (wet grinding) of this powder causes the particle size reduction giving as result the HA_{SBM} powder. The product particle size reached a x_{50} of 2.2

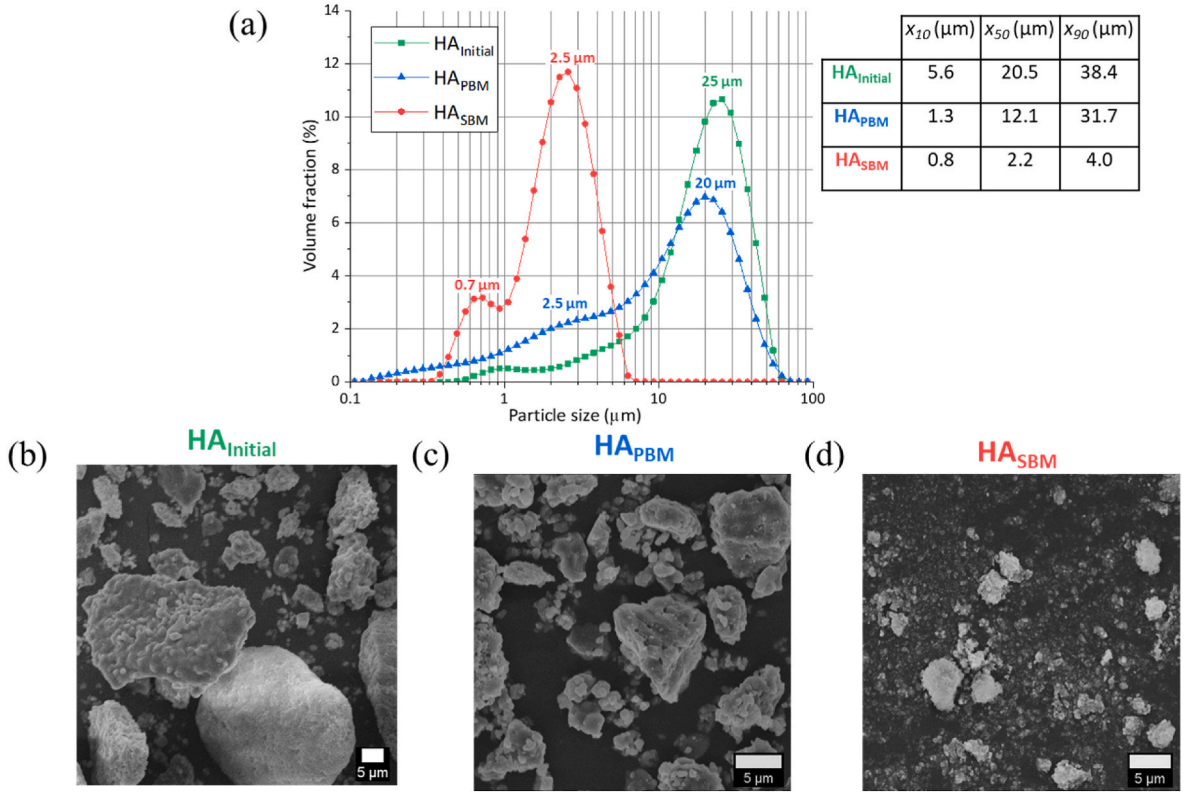

	x_{10} (μm)	x_{50} (μm)	x_{90} (μm)
$HA_{Initial}$	5.6	20.5	38.4
HA_{PBM}	1.3	12.1	31.7
HA_{SBM}	0.8	2.2	4.0

Fig. 6. (a) PSD and SEM micrographs of HA powders used in the study: (b) $HA_{Initial}$, (c) HA_{PBM}, (d) HA_{SBM}.

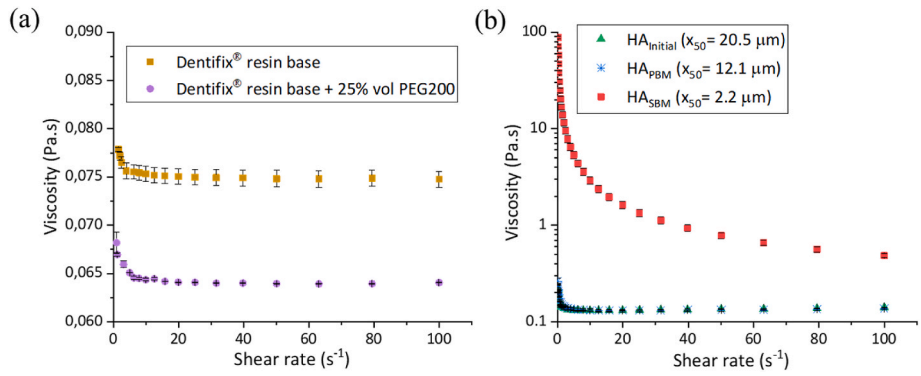

Fig. 7. (a) The flow data for Dentifix® resin base with and without the addition of 25% vol. of PEG200 as diluent. (b) The flow data for photocurable suspensions filled a 20% vol. with different HA powders ($HA_{Initial}$, HA_{PBM}, HA_{SBM}) with different median particle sizes ($HA_{Initial}$ and HA_{PBM} show very close viscosities).

µm measured in aqueous suspension (without any dispersant). The powder is formed by two particles populations, one with submicronic size (0.7 µm) and another one close to 2.5 µm.

The application of a lower energetic milling process as PBM produces a less intense particle size reduction of the $HA_{Initial}$ powder (x_{50} of 12 µm (measured in aqueous suspension)) [34]. As result, the PSD of the HA_{PBM} powder becomes more disperse with two particles populations, one of 20 µm and another one of 2.5 µm. Regarding the particles form, all three powders show irregular shapes with no noticeable variations between them.

It was observed that the surface area of the initial HA powder (6.9 $m^2.g^{-1}$) is increased after undergoing SBM process (23.8 $m^2.g^{-1}$) while after PBM process the surface area diminished (4.6 $m^2.g^{-1}$). Logically, an increase in the surface area of the powder would be expected after both milling processes because of a reduction of particle size [35]. However, the obtained values show the contrary in the case of the PBM process. This phenomenon was already observed by Granados-Correa et al. [34] in their study on the ball milling effect on tribasic calcium phosphate powders. The explanation offered by Granados-Correa et al. referred to the fact that apart from the calcium phosphate grains breakage and size diminution, the ball mill strikes induced compression of the resulting particles reducing their pore volume. It results then in a decrease in the total surface area of the powder. This theory gains reliability after the analyses of the total pore volume of powders. The values obtained were 0.017, 0.015, and 0.112 $cm^3.g^{-1}$ for $HA_{Initial}$, HA_{PBM}, and HA_{SBM} respectively, confirming the unforeseen decrease of the specific surface area of the PBM treated powder.

3.1.2. *Suspension's stability and rheology behaviour comparison*

Before starting to prepare the HA-filled suspensions, the effect of the addition of a 25% vol. of PEG200 (maximum concentration suitable without compromising the reactivity of the resin) on the rheological behaviour of the commercial organic resin base was evaluated. Fig. 7a shows the comparison between the flow curves obtained for the Dentifix® resin base before and after the addition of a 25% vol. of PEG200 compound acting as a reactive diluent. Both samples showed a shear-thinning character with a decrease in ramp average viscosity from ~0.076 Pa s to ~0.065 Pa s after the addition of the active diluent PEG200. This proportion resin/diluent was used for the preparation of all HA-filled slurries.

The flow curves obtained for suspensions containing a 20% vol. of different HA powders ($HA_{Initial}$, HA_{PBM}, HA_{SBM}) with different median particle sizes is shown in Fig. 7b. The comparison of the three viscosity-shear rate curves shows that the suspension with the highest viscosity was obtained when using the HA_{SBM} powder. It was already explained that for similar sample volume and solid concentration, smaller particle size means a higher number of particles present in the suspension, which can show Brownian motion acting against an applied shear [36,37].

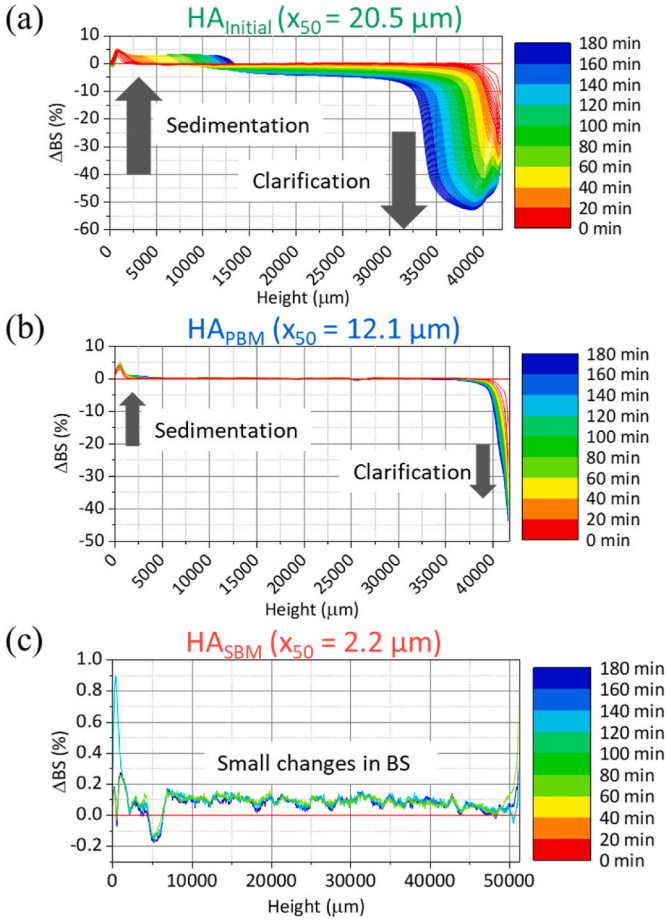

Fig. 8. Backscattering profiles of HA-filled suspensions prepared with different HA powders. (a) $HA_{Initial}$, (b) HA_{PBM}, (c) HA_{SBM} (T = 25 °C).

Since this suspension containing HA_{SBM} showed viscosity values at a low shear rate over the maximum viscosity limit for its utilization in stereolithography (5 Pa s), it was discarded as feedstock for the printing process. When comparing the viscosity-shear rate curves obtained by $HA_{Initial}$ and HA_{PBM} suspensions no big differences were observed, which could be due to the less significant variation between their PSDs.

A comparison between the stabilities of the three types of HA-filled suspensions was carried out.

Fig. 8 shows the BS profiles of the HA-filled suspensions for 3 h. The suspensions prepared with HA_{SBM} showed the highest stability since it showed almost no alteration of the BS profile during the whole time of

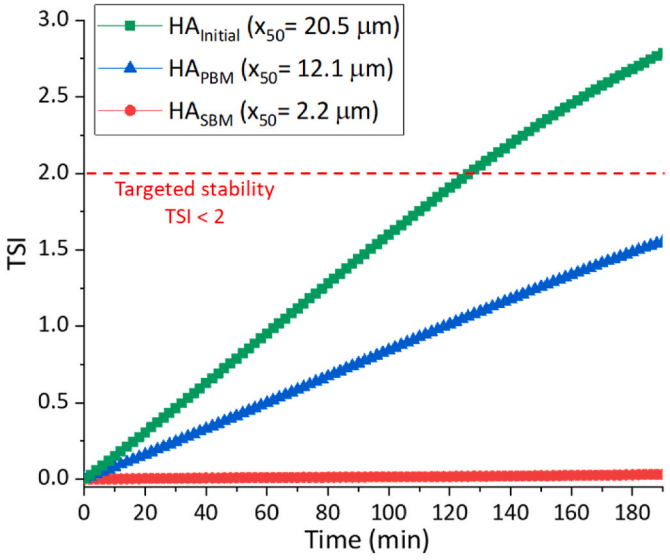

Fig. 9. TSI values of HA-filled suspensions as a function of time (T = 25 °C).

analysis. The slurries containing $HA_{Initial}$ and HA_{PBM} showed both particles sedimentation (BS increases at the bottom of the tube) and clarification (BS decreases at the top) phenomena, however, it was less pronounced in the second case. The differences between the stabilities can be due to different factors that can affect the rate of sedimentation of the prepared suspensions, such as the particle size and the viscosity of the suspensions. It is known that the smaller the particle size and higher the viscosity of a suspension, the slower will be the sedimentation rate of the particles [38]. Which, could explain the results obtained.

As mentioned in the introduction, the overall stability of slurries described as a TSI value lower than 2 was pursued for the duration of the HA parts fabrication. Fig. 9 shows the evolution of the TSI values obtained for the HA-filled slurries as a function of time.

The suspension containing the $HA_{Initial}$ powder showed the worst stability (TSI ≅ 2.75) after 3 h of the three suspensions. The highest stability was obtained by the slurry with HA_{SBM} powder constituted by the smallest particles, whose TSI value remained almost unaltered for the whole duration of the analysis. HA_{PBM} suspension showed intermedium stability with a TSI value close to 1.48 after 3 h.

The previous stability and rheological behaviour analyses allowed us to compare the properties of the suspensions prepared with different HA powders. The order for the stabilities observed for the three kinds of slurries was $HA_{SBM} \gg\gg HA_{PBM} > HA_{Initial}$ with a clear difference between the powder of finer particle size (HA_{SBM}) to the others two. However, the study of the rheology of the suspensions showed the following viscosity order for the slurries $HA_{SBM} \gg\gg HA_{PBM} \cong HA_{Initial}$. The high viscosity showed by the suspension prepared with HA_{SBM} (low shear rate viscosity >5 Pa s) hindered the homogeneous spread of the suspension to be employed as feedstock in the MSLA printer. Indeed, the apparatus employs the vertical movement of the printing stage to refill with suspension the space between the stage and the LCD screen. The poor flow of this suspension makes impossible this indispensable refilling step. For this reason, the use of this powder as filler was discarded for the production of photocurable HA-filled suspension feedstock. The suspension showing the most favourable results on suspension rheology (low shear viscosity <5 Pa s) and stability (TSI <1.5) was the one prepared with the powder HA_{PBM}. For this reason, only this powder was considered for the preparation of the highly-loaded photocurable HA-filled resins that will be used as feedstock for the production of HA scaffolds via MSLA process.

The powder concentration is known to be an important factor influencing the degree of shrinkage during the posterior debinding process. The higher the solid loading the lower the shrinkage, but a too high solid loading makes difficult the debinding process due to the impeding of the gases diffusion [24]. It is then of special interest to know the maximum concentration reachable without affecting negatively the handling and processability of the suspension as well as the debinding process. To be sure that the properties for the suspension are still valid for its utilization at higher concentration, a study of the influence of the solid volume concentration of HA_{PBM} powder in the slurry properties was carried out.

Fig. 10a shows the comparison between viscosity-shear rate curves for different HA-filled suspensions containing HA_{PBM} concentrations ranging 20–50 vol %. A shorter flow ramp was produced for the sample at 50 vol % due to geometry limitations measuring high concentrated suspensions at high shear rates. However, this ramp was enough for the comparison of the rheological behaviour between suspensions. Even if an increase in the suspension viscosity is visible when a higher solid volume concentration (50 vol %) is used for the preparation of the slurries (~2 Pa s at a shear rate of 1 s^{-1}), it did not exceed the settled maximum limit of 5 Pa s.

Regarding the suspension behaviour at different solid volume concentrations, at a concentration of 40%, we observed a transition from shear-thinning to a shear-thickening character. The behaviour of suspension changes at different volume fractions [39]. At higher concentrations, an increase of the shear rate may lead to the formation of particles clusters and jamming showing a shear thickening behaviour. The transition from shear-thinning to shear-thickening is sample-specific and is known to be controlled by factors such as particle shape and particle size [40].

Collisions between particles present in a suspension are expected. Thus, they act as obstacles, and their friction demands further shear

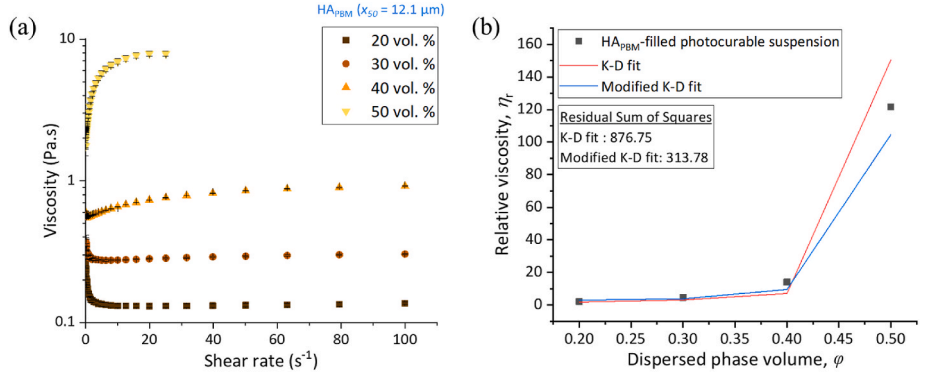

Fig. 10. (a) The viscosity-shear rate curves obtained for several HA-filled suspensions containing different HA_{PBM} concentrations. (b) Krieger-Dougherty (red line) and modified Krieger-Dougherty (blue line) fits for relative viscosities in HA_{PBM}-filled suspensions. (For interpretation of the references to colour in this figure legend, the reader is referred to the Web version of this article.)

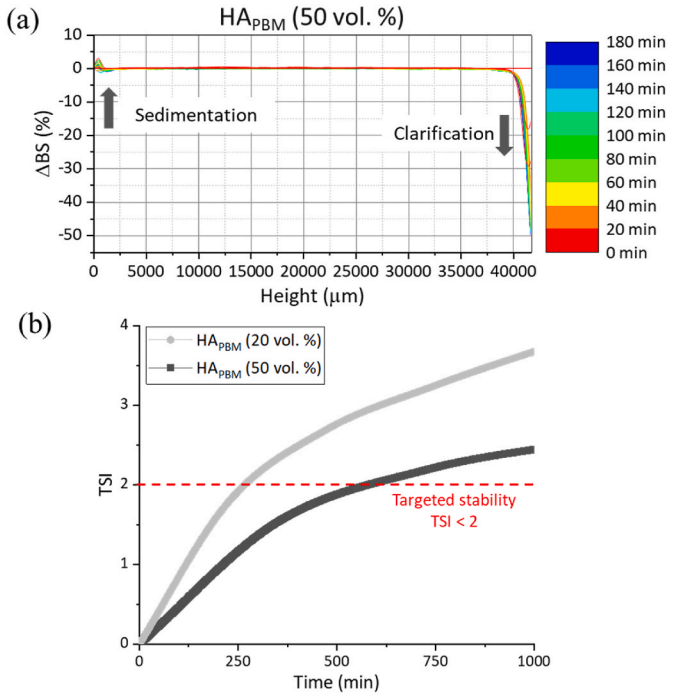

Fig. 11. (a) Backscattering profile of HA_{PBM} suspension at 50% vol. (T = 25 °C). (b) TSI values of HA_{PBM} filled suspensions at different concentrations as a function of time (T = 25 °C).

force. The higher is the solid volume fraction, the more significant the ongoing particle-particle interactions increasing the force needed to shear the suspension. This is defined as the 'crowding' effect which has been described by many semi-empirical models, however, the most popular equation was the one developed by Krieger and Dougherty (K-D) [41]:

$$\eta_r = \frac{\eta}{\eta_{medium}} = \left(1 - \frac{\varphi}{\varphi_m}\right)^{-[\eta]\varphi_m} \quad (4)$$

where η_r is the relative viscosity between η the viscosity of the suspension and η_{medium} the viscosity of the medium. φ is the volume fraction of solids in the suspension, φ_m is the maximum volume fraction of solids in the suspension (0.64 for spheres of similar size), and $[\eta]$ is the intrinsic viscosity (2.5 for spheres). Different authors have used a modified version of the K-D equation which includes the effective packing factor of ceramic powder, β, which can be determined experimentally achieving a better fitting for ceramic suspensions [42,43]. This modified version is written as follows:

$$\eta_r = \left(1 - \frac{\beta\varphi}{\varphi_m}\right)^{-[\eta]\varphi_m} \quad (5)$$

Since this analysis for correlation was out of the scope of the paper no further effort was employed on the determination of the effective packing factor of the specific suspensions under study. Instead, to perform a preliminary evaluation of the fits a value of β = 1.58 was used. This value was previously determined by Chu and Halloran [43] for HA-filled non-aqueous ceramic suspensions. A maximum volume fraction of solids in the suspension, φ_m = 0.51 was considered for the calculation. The fitting for both equations (K-D and modified K-D) to the obtained experimental values is shown in Fig. 10b. It can be observed that, still, a deeper study could be performed to obtain a better fitting between calculated and experimental values. However, between both K-D equations, the modified version showed a smaller residual sum of squares (313.78) indicating a better fit to our data.

The study of the stability of the suspension containing HA_{PBM} powder at 50 vol % is shown in Fig. 11. The phenomena occurring during the duration of the test in the suspension at 50 vol % was examined by analysing its BS profile shown in Fig. 11a. A sedimentation behaviour was observed for this suspension although less pronounced than the one observed for the suspension at a concentration of 20 vol % already seen in Fig. 8c. Fig. 11a compares the TSI values of the HA_{PBM} suspensions at 20 and 50 vol % concentrations. A lower TSI value (0.85) was observed for the slurry with a higher concentration after 180 min. It indicates higher stability compared with the slurry at a lower concentration, which shows a higher TSI (1.48) for the same duration. It took about 5 h for the suspension at 20 vol % to exceed the fixed limit of destabilization (TSI = 2), while the suspension at 50 vol % needed almost 10 h to reach this value. This confirms the principle for high concentrated suspensions showing a slow sedimentation rate [38]. The influence of sediment particle concentration on the settling velocity has been amply investigated [44,45]. It has been demonstrated that the settling velocity is lower at a higher concentration by a factor usually given by the widely used semiempirical equation offered by Richardson and Zaki [46]:

Table 2
Settling velocities of particles dispersed at different volume concentrations. n = 4.65, w = $1.04{\cdot}10^{-2}$ m s^{-1} (obtained by stokes' law).

Volume concentration (%)	w/w_m
20	2.82
30	5.25
40	$1.08{\cdot}10^{1}$
50	$2.51{\cdot}10^{1}$

$$\frac{w_m}{w} = (1 - \varphi)^n \quad (6)$$

where w ($m.s^{-1}$) is the terminal settling velocity of an individual particle in a fluid; φ is the sediment volumetric concentration (−); and w_m ($m.s^{-1}$) is the settling velocity of sediment particles dispersed at the volumetric concentration φ. n is an empirically determined exponent dependent on the particle Reynolds number R. Researchers have made an effort determining n-values to increase the accuracy of the prediction associated with equation (5) [45].

The terminal velocity of an individual particle of HA was calculated by stokes' law (w = $1.04{\cdot}10^{-2}$ m s^{-1}). Then, following equation (6), the terminal settling velocities for the HA_{PBM} particles dispersed in the photocurable resin (including diluent) at different concentrations (w_m) were obtained. The ratios between both velocities (w/w_m) at different volume concentrations are shown in Table 2. For the calculation, a laminar regime ($R < 0.2$) was considered with an n-value of 4.65. It can be observed how, for example, the settling velocity of the particles is delayed by $2.51{\cdot}10^{1}$ with a concentration of 50 vol %. Then, the decrease in settling velocity with the increase in concentration was demonstrated.

We concluded this study on the tailoring of HA powders and their influence on the suspension's properties (target properties: viscosity <5 Pa s at a shear rate 1 s^{-1} and TSI <2 for the duration of the process) by choosing the HA_{PBM}-loaded suspension at 50 vol % for its use in the MSLA process.

3.2. Printing of HA scaffolds

The suspension containing a 50% vol. of HA_{PBM} was employed for the production of the HA scaffolds following the MSLA printing and debinding-sintering procedures already described. This section will be then focused on the characterization of the parts produced. The composition of the parts will be analysed to discard any alteration of the HA phases during the process. The morphology of the parts will be evaluated through the comparison with the 3D model to analyse the possible shrinkage due to the debinding-sintering process. The

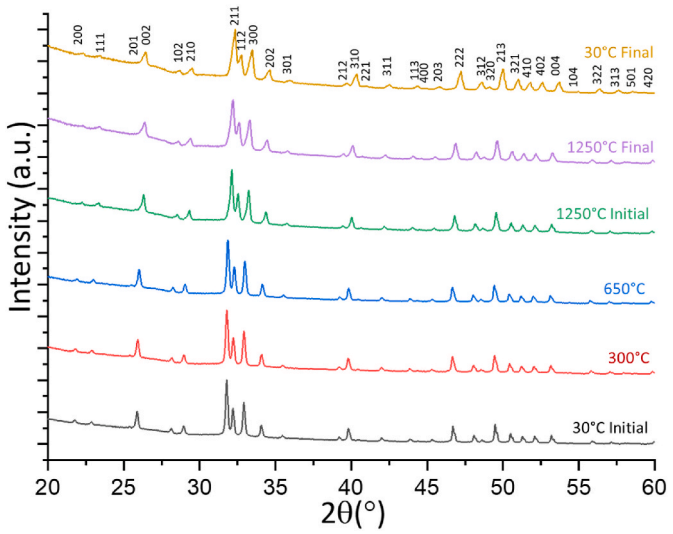

Fig. 12. In-situ XRD diffractograms of the HA scaffolds during the debinding-sintering process at different temperatures. All the diffraction peaks correspond to stoichiometric hydroxyapatite (JCPDS 00-009-0432).

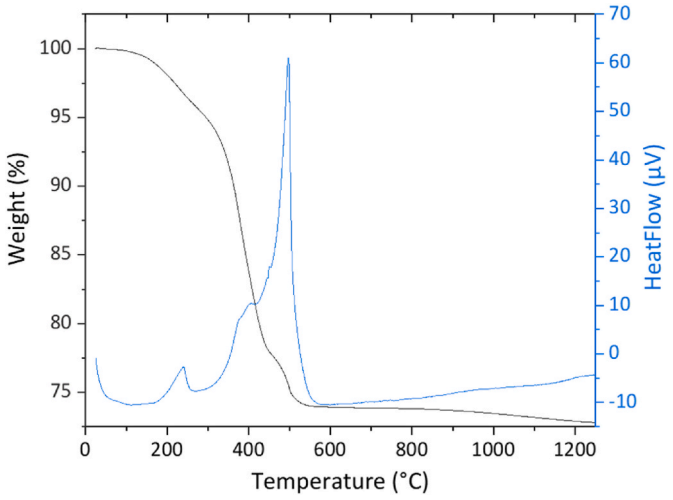

Fig. 13. Differential scanning calorimetry (DSC) and thermogravimetric analysis (TGA) of HA green body scaffold. (For interpretation of the references to colour in this figure legend, the reader is referred to the Web version of this article.)

bioactivity will be examined through the standard analysis of the dissolution rate of the part. Then the mechanical properties of the parts will be assessed to evaluate the anisotropy behaviour caused due to change in build orientation.

3.2.1. Composition

To confirm the crystalline phases of the sintered scaffolds XRD analyses were carried out. The analyses were performed at different temperatures reproducing the debinding-sintering temperature pattern to study the evolution of the phase. Fig. 12 shows the in-situ XRD diffractogram of the HA scaffold obtained at different temperatures under air atmosphere. The absence of secondary crystalized calcium phosphate phases was confirmed and only the stoichiometric hydroxyapatite phase (JCPDS 00-009-0432) was observed before, during, and after the debinding-sintering process [47]. This result confirms the thermal stability reported for HA in literature [48,49], indicating stability up to 1350 °C when it starts to decompose into other calcium phosphate phases such as tricalcium phosphate, and tetracalcium phosphate that could affect negatively the properties of the printed parts (different dissolution rates in physiological conditions, uneven grain growth …) [50]. It is known that the densification of HA reaches a saturation limit between ~1100 and 1300 °C with closed porosity [50].

Since the hydroxyapatite used was initially well crystallized, non-alteration of its crystallinity was observed. However, a decrease in the spectra intensity or resolution can be noticed after reaching 1250 °C. It was attributed to the loss of signal due to the movement in the z-axis of the sample during the in-situ measurement caused for the shrinkage of the part due to the pyrolysis of the resin and sintering.

Characterization of the cured resin with HA powder was performed by differential scanning calorimetry (DSC) and thermogravimetric analysis (TGA) to better understand the thermal treatments, especially the critical process of debinding. This characterization gives information on weight loss and involved energy during the debinding and sintering processes. The purpose of this study is to analyse the thermal degradation of the cured resin in the HA scaffold green body under air atmosphere. The TGA and DSC results for cured green body HA scaffold, optimized at 25 wt % (base resin + PEG200 diluent) and 75 wt % HA_{PBM} powder is shown in Fig. 13. The curve represents the weight loss and the energy involved during the thermal treatment, at a constant heating rate of 10 °C.min^{-1} from room temperature until 1250 °C in air atmosphere.

Three main weight loss stages can be distinguished related to the formation of volatiles, which diffuse from the interior of the part to the outside. These events represent the most critical temperature ranges during the debinding process since they indicate the escape of the gases generated and the probability of cracking of the green body.

- The first stage finishes at 240 °C with a 3 wt % of weight loss indicated by an exothermic peak, which was related to the loss of physically adsorbed water. At the same time, some organic matter such as acrylate resin or PEG200 experience soften, melt, and crack [25].
- The second stage is observed from 240 °C to 498 °C corresponding to the highest rate of weight loss, removing 22 wt % of the material. This was related to the thermal decomposition of the photocurable resin, including carbon-containing compounds [51]. Some organic components were burned and carbonized step by step.
- The third stage was defined as the thermal oxidation of the carbonized residue which does not substantially consume heat and has a minor influence on the TGA analysis [25]. When the temperature reached 1200 °C, the mass curve tended to be stable.

Two exothermic events were detected, associated with the three weight-loss events. Thus, indicating that the thermal degradation of the

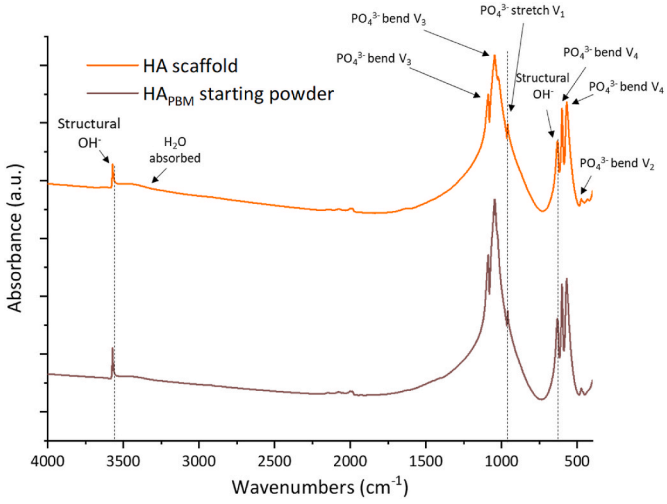

Fig. 14. FTIR spectrum analysis of the HA before and after the SD process.

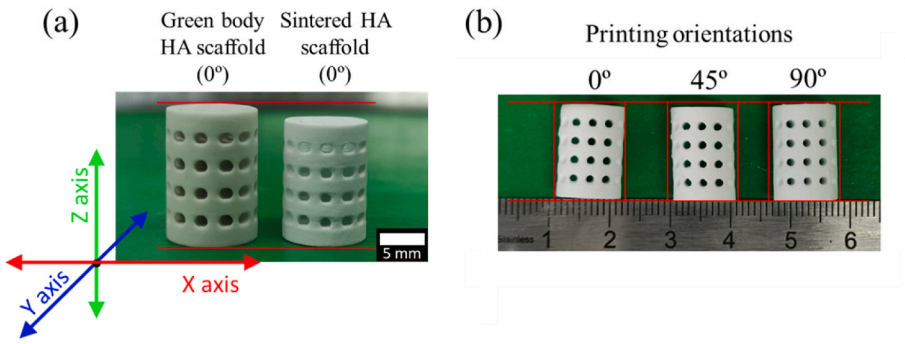

Fig. 15. Visual examination of HA parts: (a) comparison between green body and sintered HA scaffolds (including axes arrows), (b) comparison between sintered HA scaffolds printed at three different orientations (0°, 45°, and 90°). (For interpretation of the references to colour in this figure legend, the reader is referred to the Web version of this article.)

Table 3
Average shrinkage in x-y and z-axis of parts after the debinding-sintering process for each of the three printing orientations. Average porosity and relative densities of sintered HA scaffolds determined by different methods. (N = 10).

Printing orientation (°)	Average shrinkage x-y axes (%)	Average shrinkage z-axis (%)	Total porosity (CT) (% vol.)	Total porosity (Hg) (%vol.)	Relative density (Archimedes) ($g.cm^{-3}$)	Relative density (Geometrical) ($g.cm^{-3}$)
0	5.33 ± 0.07	9.72 ± 0.07	31.4	35.8	2.84 ± 0.04	2.31 ± 0.13
45	6.20 ± 0.02	7.13 ± 0.05	30.6	35.5	2.84 ± 0.01	2.31 ± 0.66
90	7.72 ± 0.03	5.09 ± 0.04	32.7	35.6	2.85 ± 0.02	2.25 ± 0.52

resin used for the suspensions releases energy during the thermal process. Indeed, the most intense exothermic peak is related to the weight loss event corresponding to the degradation of the carbon-containing compounds during the polymer degradation. On the whole, total organic removal is observed with a weight loss of ~25 wt %. It is important to point out that the heating rates used during the debinding-sintering process of the scaffolds are between 10 and 5 times lower than the used for the TGA and DSC analyses. It is expected to produce deeper pyrolysis of the polymeric phase and at the same time control the diffusion of gases avoiding the formation of cracks. The results obtained for the thermal analyses are in correlation with the observed in literature for similar resin photocurable thermal degradation studies [21,25,51].

A FTIR analysis was performed to confirm the compounds present in the parts after the whole production process. For comparison, the powder (HA_{PBM}) used as filler during the preparation of the slurry was also analysed. Fig. 14 shows the FTIR spectra of the starting powder and the HA scaffold produced. Small variations can be noticed between them. In both spectra the PO_4^{3-} and structural OH^- vibration bands corresponding to HA are clearly visible at 1092 cm^{-1}, 1040 cm^{-1}, 962 cm^{-1}, 601 cm^{-1}, 575 cm^{-1}, 561 cm^{-1}, and at 650 cm^{-1}, 3600 cm^{-1} [47]. No secondary species were detected before or after the whole HA scaffold production process.

3.2.2. *Macro-structural properties and physical changes of sintered HA scaffolds*

HA bioceramic scaffolds were examined to evaluate their macro-structural properties (surface finishing, porosity, and density) and physical changes (shrinkage) after the debinding-sintering process. Fig. 15 shows the photographs of the green body and sintered HA scaffolds produced by the MSLA process. Fig. 15a shows the differences in dimension between the green body scaffold and its homologous after the debinding-sintering process due to the pyrolysis-induced shrinking. However, no fracture or crack was detected after the debinding-sintering process. Fig. 15b shows differences between the dimensions of the scaffolds printed at different orientation angles (shrinkage values can be observed in Table 3). The differences in dimension were only observed once the parts were submitted to the debinding-sintering process. It indicates a physical anisotropic effect produced by the shrinkage which depends on the orientation in which the layers forming the part was printed. This kind of anisotropic physical change has been reported in previous studies on the 3D printing of ceramic parts [21,52].

Table 3 shows the general information related to the macro-structural properties of the produced HA scaffolds. The calculated average pyrolysis-induced shrinkage shows that there is a different effect depending on the axis. For parts printed at the same orientation, a higher distortion effect was measured for the axes perpendicular to the printing direction (e.g., z-axis for parts printed at 0° or x-y plane).

No big differences in the total porosity were observed between the three orientations. A higher porosity was obtained when using the Hg intrusion porosimetry method, this could indicate that the resolution of the CT analysis (9 μm) was not enough to take into account the micro-porosity. The total porosity of the scaffolds is close to the common cancellous bone porosity of 50–90% [53].

Almost similar relative densities were obtained for the three kinds of scaffolds (2.84 g cm^{-3}) demonstrating a good capability of the MSLA technique in the reproduction of HA scaffolds with an accurate controlled and interconnected macroporosity. The obtained density is lower than the hydroxyapatite density (3.16 g cm^{-3}), thus corresponding to the expected values for a scaffold with open and close porosity.

The SEM micrographs of the HA scaffolds surface printed at three different orientations are shown in Fig. 16. SEM micrographs were taken at a similar X-Z plane (front view) of the parts for comparison. The macroporosity of the scaffolds is composed of an interconnected porosity with a pore size of about 1000 μm. This result fulfils the objective of producing scaffolds with controlled macroporosity (pore size >400 μm) which could promote the attachment, growth, and proliferation of bone cells inside of the scaffold enhancing the new bone formation and the formation of capillaries. This macro-porosity should then provide transport pathways for oxygen, wastes, and nutrients necessary to maintain living cells [54,55]. Different surface finishing is observed in this plane depending on the printing orientation with a clear view of the layers for the scaffolds printed at 0° and 45°. However, no significant pores in the microstructures can be observed due to any delamination or imperfect bonding between layers. This indicates a good sinterability of the HA powder.

Additionally, to analyse the internal microstructure of the HA

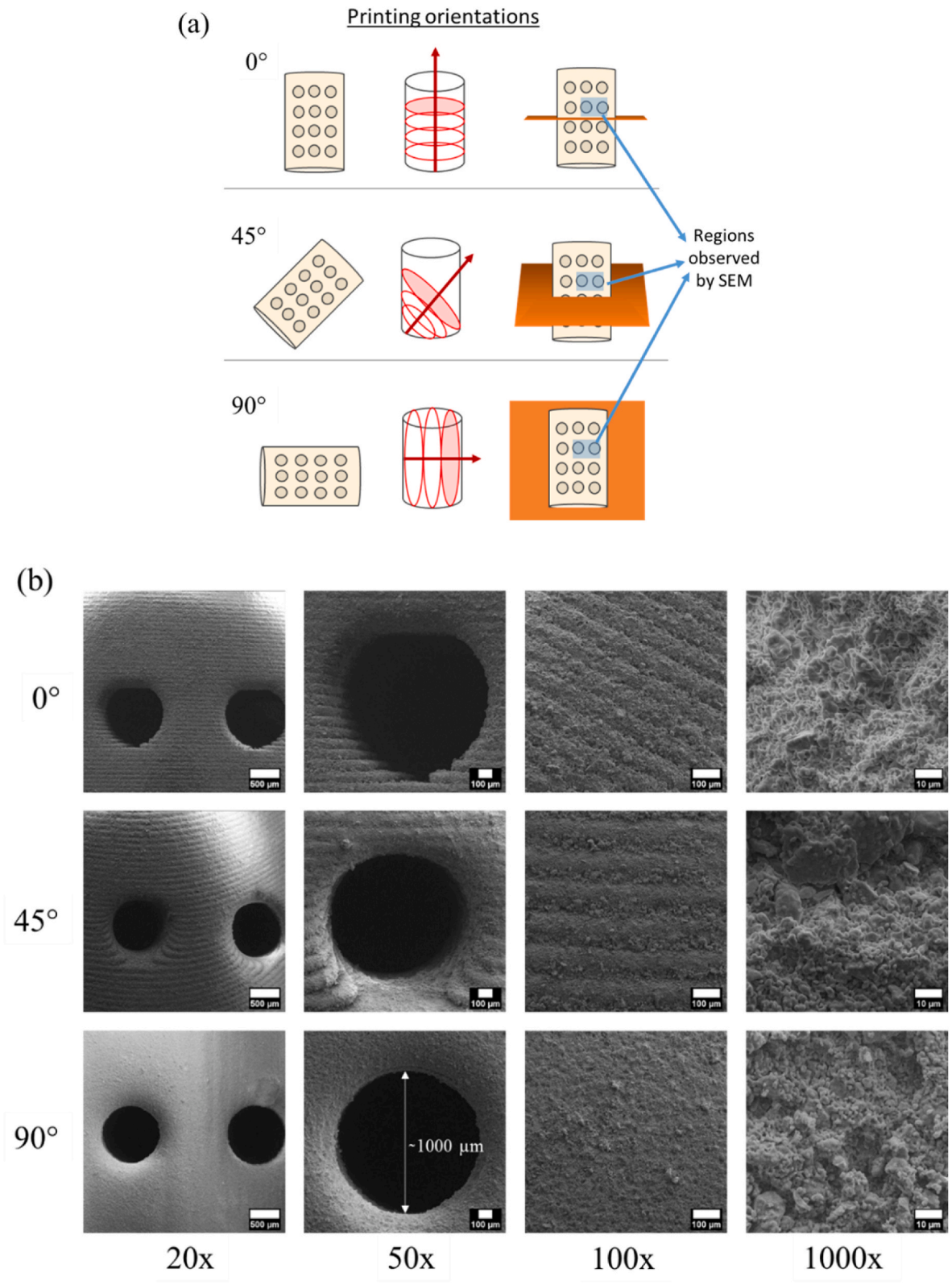

Fig. 16. (a) Three different schematic representations of the three printing orientations employed. (b) SEM micrographs at different magnifications of the HA scaffolds (X, Z plane) printed at three different orientations.

scaffolds the cross-section at the X–Y plane (top view) was observed by SEM. These micrographs are shown in Fig. 17. From a general view, no induced anisotropy was identified due to the printing process on the three types of scaffolds. The three samples presented micropores of about 10–15 µm of diameter corresponding to the microstructural porosity of the sintered HA. This porosity could allow the migration and proliferation of osteoblasts (15–50 µm), and especially stem cells (5–12 µm). The HA crystal sizes correspond with the particle size of the HA_{PBM} powder used for the preparation of the scaffolds. A dispersed distribution of HA grains was observed with sizes from 2.5 µm to 20 µm of

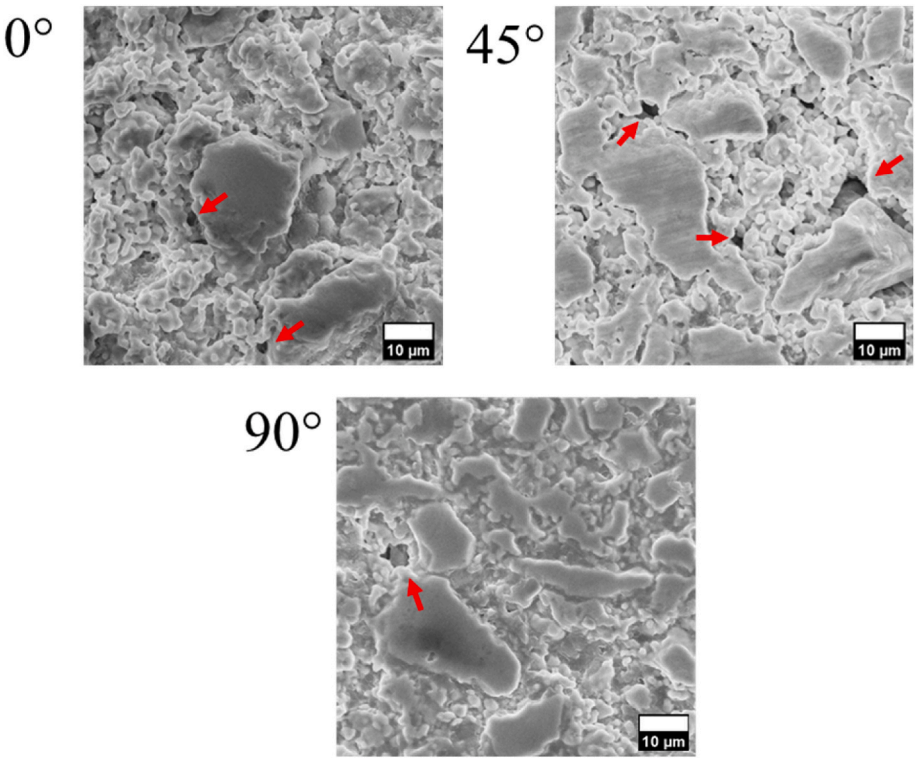

Fig. 17. Cross-section of parts of the HA scaffolds (X, Y plane) printed at three different orientation degrees. Micropores are remarked by red arrows. (For interpretation of the references to colour in this figure legend, the reader is referred to the Web version of this article.)

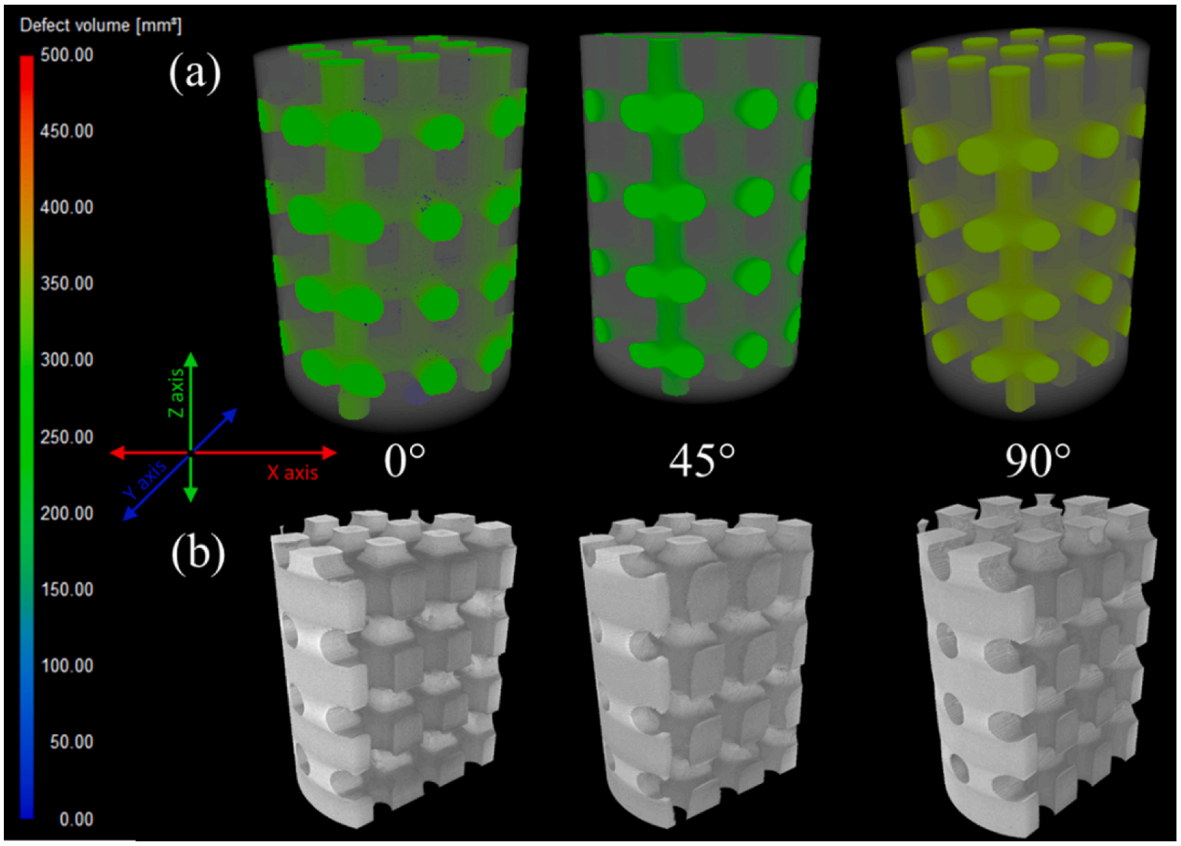

Fig. 18. Visualization obtained using X-ray micro-computed tomography of the three kinds of HA scaffolds (0°, 45°, and 90°) produced by MSLA after the debinding-sintering treatment. (a) The pore distribution of HA scaffolds with previously modelled interconnected macroporosity and circular overtures of 1000 µm in the three directions. (b) Cross-section views of HA scaffolds in X–Y, and Y-Z planes.

Table 4
Compressive strength of HA scaffolds depending on the printing orientation. (N = 10).

Printing orientation (°)	Compression strength (MPa)
0	4.2 ± 0.4
45	4.9 ± 0.3
90	4.8 ± 0.2

diameter.

Three-dimensional reconstructions of the sintered scaffolds using X-ray micro-computed tomography are also illustrated in Fig. 18. A defect volume scale was added for a better comparison of the pore volume. The three samples showed accurate controlled and interconnected macro-porosity with a total volume in the range of 300–350 mm^3. The cross-section views of HA scaffolds in X–Y and Y-Z planes did not show any kind of anisotropy induced by the MSLA process. This homogeneity observed for the whole volume of the parts indicates suitability for the processing of suspensions by MSLA technique on the production of HA scaffolds with controlled macroporosity. Additional CT results showing the internally interconnected porosity of the scaffold printed at 0° can be found in Fig. S1.

3.2.3. Mechanical properties

The anisotropic effect of the printing orientation on the scaffolds mechanical properties was examined. Table 4 shows the compression strength of the sintered scaffolds as a function of the orientation in which they were printed. Mechanical strength is primarily controlled by pore volume and distribution, however, in this case, the total porosity of the scaffolds has been demonstrated to not be affected by the printing orientation. Thus, the total pore volume of the samples studied was almost similar (Table 3). Scaffolds with 0° orientation are weakest in compressive strength (4.3 ± 0.4 MPa) since the plane in which they are printed is perpendicular to the direction of load. With the inclination of the plane, it becomes diagonal to the loading direction (45°) resisting more compressive load (4.9 ± 0.3 MPa). Then, a decrease in the compressive load is observed for (90°) as the printing orientation is parallel to the direction of loading (4.8 ± 0.2 MPa). These results are in line with Lee et al. [56] and Saini et al. [57] which said that the diagonally printed specimens (45°) have higher compressive strength as compared to axial and transverse 3D printed parts. Indeed, they are in accordance with the results obtained by Feng et al. [21] whose HA printed scaffolds (at orientation 0° and using a 50 vol % suspension) with higher porosity than the ones produced in the present study showed lower compressive strength. The values obtained for the three types of scaffolds are found to be within the range of values reported for cancellous bone compressive strength (1–12 MPa) for porosity between 50 and 90%. Then, to advance this study, the porosity of the scaffolds (~31%) could be increased to reproduce closer conditions [53].

The compressive stress-strain curves obtained for the bioceramic HA scaffolds printed at 45° are shown in Fig. S2a. These curves are characterized by an initial non-linear toe region (first strain stage) followed by a main linear region till the failure point. The inexistence of a concave shape before the failure point and the sharp peaks are common in brittle materials as ceramics. It is known that brittle materials, when subjected to stress, break with little elastic deformation and without significant plastic deformation. For this reason, brittle materials absorb relatively little energy before the fracture, even those of high strength [58]. Cracks propagate rapidly along the compression loading direction as shown in Fig. S2b. The fluctuations (or serration) in the compression stress-strain response are essentially attributed to the spalling of a small specimen volume, as the growing cracks either meet the free/unconstrained surface of the material or, coalesce between them [59]. This is consistent with other works in the literature [21,52]. Brittle fracture with a transgranular cleavage is observed (cracks grow through the material grains) and no apparent plastic deformation takes place before fracture. No preferred direction was observed for the fracture as an effect of the orientation in which the specimens were printed.

3.2.4. Dissolution rate

The *in vitro* behaviour of the sintered HA scaffolds was preliminarily evaluated in terms of dissolution rate, Ca^{2+} ion release, and pH change of the dissolution medium (0.05 M TRIS buffer solution) at 37±1 °C. The pH value evolution of the TRIS buffer solution is shown in Fig. 19a. The initial pH of the TRIS buffer solution was 7.3. Then, this value was decreasing with the increase of the HA scaffold soaking time. After 72 h the pH reached a value of 7.24. The pH variation surrounding an implant is an indicator of the *in vivo* degradation. A fast unintentional degradation in contact with the environment can deteriorate the mechanical properties of the implant [60]. In this case, a low variation of the pH was observed (lower than ±0.3) indicating a low degradation of the HA scaffold. The scaffold weight loss and Ca^{2+} ion concentrations in the solution at different soaking times are given in Fig. 19b. A slight weight loss of the HA scaffolds was observed after 24 h. It increased with the soaking time until a 0.12% of loss of the total scaffold mass at 72 h. In addition, a low Ca^{2+} ion release (1.26 mg l^{-1}) was observed during the time of the measurement. These results were attributed to the high crystallinity of the HA phase (due to the sintering process) which is known to decrease the dissolution rate [61].

It is known that depending on the calcium phosphate phase the dissolution rate varies, being HA one of the phases showing low rates [62]. Some phases like TCP may dissolve fast and replace the coating or cement with bone. This property depends on the calcium phosphate phase content of the scaffold, crystallinity, particle size, and porosity. A higher degree of porosity means a higher surface area in contact between the implant and the body fluids, inducing a faster dissolution rate. Then, a higher degree of crystallinity of the calcium phosphate structure can reduce the solubility of the scaffolds, thus explaining the large differences in solubility between scaffolds prepared with the same calcium phosphate phase [61,63]. The rate of bone substitution also depends on the age, sex, and general metabolic health of the recipient, even on the

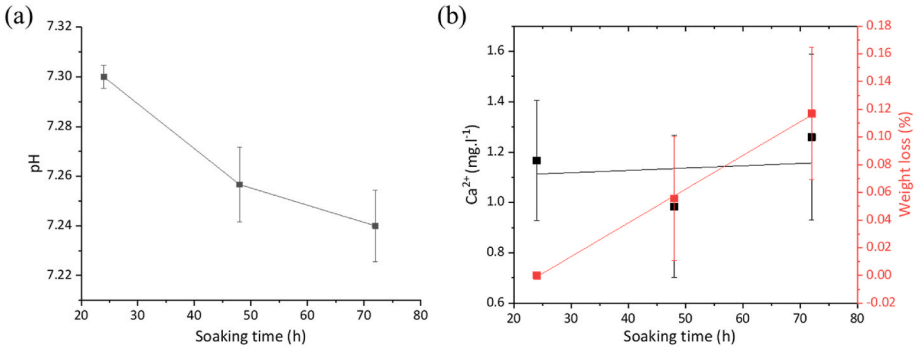

Fig. 19. (a) TRIS solution pH evolution, (b) Ca^{2+} ion release, and scaffold weight loss evolution as a function of the sintered HA scaffold soaking time. (N = 3).

anatomic site, thus the desired resorption rate is the rate comparable to the formation of bone tissue (between a few months and a few years), in the case of calcium phosphate it may take 3–36 months to be replaced by bone [64].

4. Conclusions

In the present work, HA scaffolds were obtained by MSLA innovative AM process. HA powders with different characteristics were produced and employed for the preparation of HA-filled photocurable suspensions. The influence of the different powders on the properties of suspensions was evaluated. After a comparison of the rheological behaviour and dispersion stability of the suspensions, it was found that the powder tailored through the planetary ball mill process having an intermedium particle size showed the most outstanding results (viscosity <5 Pa s at a shear rate 1 s^{-1} and TSI <2 for the duration of the process) at 50 vol %. The processability of suspensions was tested in a commercial MSLA apparatus through the production of scaffolds with controlled macroporosity. The process showed high accuracy in producing the macroporosity (pore size of 1000 μm) at three printing orientations (0°, 45°, and 90°). A debinding-sintering process at 1250 °C was employed for the complete pyrolysis of the resin and sintering of the scaffold. The chemical composition and macro-structural properties of the scaffolds were examined. It was observed that the debinding-sintering shrinkage of the parts was dependent on the printing orientation, with a higher shrinkage in the direction perpendicular to the printed plane. The analysis of the mechanical properties also showed a slight anisotropic effect induced by the printing orientation with the highest compressive strength (4.9 ± 0.3 MPa) obtained for the scaffolds printed diagonally (45°). Then, the dissolution rate test of the scaffolds showed a low variation in the TRIS solution pH with the soaking time and a slow dissolution rate, which was attributed to the high crystallinity and intrinsic stability of the HA calcium phosphate phase. In conclusion, the tailoring of HA powder suitable for its use as a filler in photocurable suspensions was confirmed. The HA specimens produced showed promising results for their use in surgery for guided bone regeneration in the case of minor or non-load bearing voids requiring slow resorption properties.

Data availability

The raw/processed data required to reproduce these findings cannot be shared at this time as the data also forms part of an ongoing study.

Declaration of interests

The authors declare that they have no known competing financial interests or personal relationships that could have appeared to influence the work reported in this paper.

Acknowledgements

DOC-3D-Printing project has received funding from the European Union's Horizon 2020 research and innovation programme under the Marie Skłodowska-Curie grant agreement No 764935.

Appendix A. Supplementary data

Supplementary data to this article can be found online at https://doi.org/10.1016/j.oceram.2022.100235.

References

[1] Ageing Europe - statistics on population developments. https://ec.europa.eu/eurostat/statistics-explained/index.php?title=Ageing_Europe_-_statistics_on_population_developments, 2020.
[2] Office of the Surgeon General (US), Bone Health and Osteoporosis: A Report of the Surgeon General, Office of the Surgeon General (US), Rockville (MD), 2004. http://www.ncbi.nlm.nih.gov/books/NBK45513/.
[3] I. Benjumeda Wijnhoven, R. Vallejos, J.F. Santibanez, C. Millán, J.F. Vivanco, Analysis of cell-biomaterial interaction through cellular bridge formation in the interface between hGMSCs and CaP bioceramics, Sci. Rep. 10 (2020) 16493, https://doi.org/10.1038/s41598-020-73428-y.
[4] D.W. Hutmacher, Scaffolds in tissue engineering bone and cartilage, Biomaterials 21 (2000) 2529–2543, https://doi.org/10.1016/S0142-9612(00)00121-6.
[5] L. Zhang, Y. Morsi, Y. Wang, Y. Li, S. Ramakrishna, Review scaffold design and stem cells for tooth regeneration, Japanese Dental Science Review 49 (2013) 14–26, https://doi.org/10.1016/j.jdsr.2012.09.001.
[6] H. Schliephake, F.W. Neukam, Bone replacement with porous hydroxyapatite blocks and titanium screw implants: an experimental study, J. Oral Maxillofac. Surg. 49 (1991) 151–156, https://doi.org/10.1016/0278-2391(91)90103-S.
[7] B.A. Gultekin, E. Bedeloglu, T.E. Kose, E. Mijiritsky, Comparison of bone resorption rates after intraoral block bone and guided bone regeneration augmentation for the reconstruction of horizontally deficient maxillary alveolar ridges, BioMed Res. Int. 2016 (2016), e4987437, https://doi.org/10.1155/2016/4987437.
[8] M. Tumedei, P. Savadori, M. Del Fabbro, Synthetic blocks for bone regeneration: a systematic review and meta-analysis, Int. J. Mol. Sci. 20 (2019) 4221, https://doi.org/10.3390/ijms20174221.
[9] A. Monje, H.-L. Wang, Biological and Physical Properties of Bone Block Grafting Biomaterials for Alveolar Ridge Augmentation, (n.d.) 14.
[10] J.T. Mellonig, Bone allografts in periodontal therapy, Clin. Orthop. Relat. Res. (1996) 116–125, https://doi.org/10.1097/00003086-199603000-00014.
[11] E. Pamula, E. Filová, L. Bačáková, V. Lisá, D. Adamczyk, Resorbable polymeric scaffolds for bone tissue engineering: the influence of their microstructure on the growth of human osteoblast-like MG 63 cells, J. Biomed. Mater. Res. 89A (2009) 432–443, https://doi.org/10.1002/jbm.a.31977.
[12] A. Kurella, N.B. Dahotre, Review paper: surface modification for bioimplants: the role of laser surface engineering, J. Biomater. Appl. 20 (2005) 5–50, https://doi.org/10.1177/0885328205052974.
[13] H. Qu, Additive manufacturing for bone tissue engineering scaffolds, Mater. Today Commun. 24 (2020) 101024, https://doi.org/10.1016/j.mtcomm.2020.101024.
[14] H.H. Yen, P.G. Stathopoulou, CAD/CAM and 3D-printing applications for alveolar ridge augmentation, Curr. Oral Health Rep. 5 (2018) 127–132, https://doi.org/10.1007/s40496-018-0180-4.
[15] L.C. Hwa, S. Rajoo, A.M. Noor, N. Ahmad, M.B. Uday, Recent advances in 3D printing of porous ceramics: a review, Curr. Opin. Solid State Mater. Sci. 21 (2017) 323–347, https://doi.org/10.1016/j.cossms.2017.08.002.
[16] K. Lin, R. Sheikh, S. Romanazzo, I. Roohani, 3D printing of bioceramic scaffolds—barriers to the clinical translation: from promise to reality, and future perspectives, Materials 12 (2019) 2660, https://doi.org/10.3390/ma12172660.
[17] S. Zakeri, M. Vippola, E. Levänen, A comprehensive review of the photopolymerization of ceramic resins used in stereolithography, Addit. Manuf. 35 (2020) 101177, https://doi.org/10.1016/j.addma.2020.101177.
[18] J.R. Zyzalo, Masked Projection Stereolithography: Improvement of the Limaye Model for Curing Single Layer Medium Sized Parts, 2008, p. 274.
[19] H. Quan, T. Zhang, H. Xu, S. Luo, J. Nie, X. Zhu, Photo-curing 3D printing technique and its challenges, Bioact. Mater. 5 (2020) 110–115, https://doi.org/10.1016/j.bioactmat.2019.12.003.
[20] X. Li, Y. Yuan, L. Liu, Y.-S. Leung, Y. Chen, Y. Guo, Y. Chai, Y. Chen, 3D printing of hydroxyapatite/tricalcium phosphate scaffold with hierarchical porous structure for bone regeneration, Bio-Des. Manuf. 3 (2020) 15–29, https://doi.org/10.1007/s42242-019-00056-5.
[21] C. Feng, K. Zhang, R. He, G. Ding, M. Xia, X. Jin, C. Xie, Additive manufacturing of hydroxyapatite bioceramic scaffolds: dispersion, digital light processing, sintering, mechanical properties, and biocompatibility, J. Adv. Ceram. 9 (2020) 360–373, https://doi.org/10.1007/s40145-020-0375-8.
[22] K. Zhang, C. Xie, G. Wang, R. He, G. Ding, M. Wang, D. Dai, D. Fang, High solid loading, low viscosity photosensitive Al2O3 slurry for stereolithography based additive manufacturing, Ceram. Int. 45 (2019) 203–208, https://doi.org/10.1016/j.ceramint.2018.09.152.
[23] S.Y. Song, M.S. Park, D. Lee, J.W. Lee, J.S. Yun, Optimization and characterization of high-viscosity ZrO2 ceramic nanocomposite resins for supportless stereolithography, Mater. Des. 180 (2019) 107960, https://doi.org/10.1016/j.matdes.2019.107960.
[24] M. Pfaffinger, G. Mitteramskogler, R. Gmeiner, J. Stampfl, Thermal debinding of ceramic-filled photopolymers, MSF 825–826 (2015) 75–81. https://doi.org/10.4028/www.scientific.net/MSF.825-826.75.
[25] Q. Chen, B. Zou, Q. Lai, Y. Wang, R. Xue, H. Xing, X. Fu, C. Huang, P. Yao, A study on biosafety of HAP ceramic prepared by SLA-3D printing technology directly, J. Mech. Behav. Biomed. Mater. 98 (2019) 327–335, https://doi.org/10.1016/j.jmbbm.2019.06.031.
[26] F.P.W. Melchels, J. Feijen, D.W. Grijpma, A review on stereolithography and its applications in biomedical engineering, Biomaterials 31 (2010) 6121–6130, https://doi.org/10.1016/j.biomaterials.2010.04.050.
[27] H. Li, Y. Liu, Y. Liu, K. Hu, Z. Lu, J. Liang, Effects of solvent debinding on the microstructure and properties of 3D-printed alumina ceramics, ACS Omega 5 (2020) 27455–27462, https://doi.org/10.1021/acsomega.0c03944.
[28] M. Tourbin, F. Brouillet, B. Galey, N. Rouquet, P. Gras, N. Abi Chebel, D. Grossin, C. Frances, Agglomeration of stoichiometric hydroxyapatite: impact on particle size distribution and purity in the precipitation and maturation steps, Powder Technol. 360 (2020) 977–988, https://doi.org/10.1016/j.powtec.2019.10.050.

[29] M.A. Inam, S. Ouattara, C. Frances, Effects of concentration of dispersions on particle sizing during production of fine particles in wet grinding process, Powder Technol. 208 (2011) 329–336, https://doi.org/10.1016/j.powtec.2010.08.025.
[30] P. Navarrete-Segado, Tailoring calcium phosphate powder properties for additive manufacturing, PhD thesis, INPT, Toulouse, 2021, http://www.theses.fr/s210200. (Accessed 10 October 2021).
[31] Phrozen Shuffle & Shuffle XL User Manuals, Dropbox paper. (n.d.). https://phrozen3d.com/pages/manual.
[32] V. Raikos, Encapsulation of vitamin E in edible orange oil-in-water emulsion beverages: influence of heating temperature on physicochemical stability during chilled storage, Food Hydrocolloids 72 (2017) 155–162, https://doi.org/10.1016/j.foodhyd.2017.05.027.
[33] C.A. Schneider, W.S. Rasband, K.W. Eliceiri, NIH Image to ImageJ: 25 years of image analysis, Nat. Methods 9 (2012) 671–675, https://doi.org/10.1038/nmeth.2089.
[34] F. Granados-Correa, J. Bonifacio-Martínez, J. Serrano-Gómez, The ball milling effect on tribasic calcium phosphate and its chromium (VI) ion sorption properties, J. Chil. Chem. Soc. 54 (2009), https://doi.org/10.4067/S0717-97072009000300010. Journal of The Chilean Chemical Society.
[35] P.L. Guzzo, J.B. Santos, R.C. David, Particle size distribution and structural changes in limestone ground in planetary ball mill, Int. J. Miner. Process. 126 (2014) 41–48, https://doi.org/10.1016/j.minpro.2013.11.005.
[36] R. Newburgh, J. Peidle, W. Rueckner, Einstein, Perrin, and the reality of atoms: 1905 revisited, Am. J. Phys. 74 (2006), https://doi.org/10.1119/1.2188962. American Journal of Physics.
[37] D. Komissarenko, P. Sokolov, A. Evstigneeva, I. Shmeleva, A. Dosovitsky, Rheological and curing behavior of acrylate-based suspensions for the DLP 3D printing of complex Zirconia parts, Materials 11 (2018) 2350, https://doi.org/10.3390/ma11122350.
[38] M. Nutan, I. Reddy, General principles of suspensions, in: Pharmaceutical Suspensions: from Formulation Development to Manufacturing, 2009, pp. 39–65, https://doi.org/10.1007/978-1-4419-1087-5_2.
[39] D. Quemada, Rheological modelling of complex fluids. I. The concept of effective volume fraction revisited, Eur. Phys. J. AP. 1 (1998) 119–127, https://doi.org/10.1051/epjap:1998125.
[40] J.J. Stickel, R.L. Powell, Fluid mechanics and rheology of dense suspensions, Annu. Rev. Fluid Mech. 37 (2005) 129–149, https://doi.org/10.1146/annurev.fluid.36.050802.122132.
[41] I.M. Krieger, T.J. Dougherty, A mechanism for non-Newtonian flow in suspensions of rigid spheres, Trans. Soc. Rheol. 3 (1959) 137–152, https://doi.org/10.1122/1.548848.
[42] V. Tomeckova, J.W. Halloran, Flow behavior of polymerizable ceramic suspensions as function of ceramic volume fraction and temperature, J. Eur. Ceram. Soc. 31 (2011) 2535–2542, https://doi.org/10.1016/j.jeurceramsoc.2011.01.019.
[43] T.-M.G. Chu, J.W. Halloran, High-temperature flow behavior of ceramic suspensions, J. Am. Ceram. Soc. 83 (2004) 2189–2195, https://doi.org/10.1111/j.1151-2916.2000.tb01534.x.
[44] T.E. Baldock, M.R. Tomkins, P. Nielsen, M.G. Hughes, Settling velocity of sediments at high concentrations, Coast Eng. 51 (2004) 91–100, https://doi.org/10.1016/j.coastaleng.2003.12.004.
[45] N.-S. Cheng, Effect of concentration on settling velocity of sediment particles, J. Hydraul. Eng. 123 (1997) 728–731. https://doi.org/10.1061/(ASCE)0733-9429(1997)123:8(728).
[46] J.F. Richardson, W.N. Zaki, Sedimentation and fluidisation. Part 1, Trans. Inst. Chem. Eng. 32 (1954) 35–53.
[47] C. Rey, O. Marsan, C. Combes, C. Drouet, D. Grossin, S. Sarda, Characterization of calcium phosphates using vibrational spectroscopies, in: B. Ben-Nissan (Ed.), Advances in Calcium Phosphate Biomaterials, Springer Berlin Heidelberg, Berlin, Heidelberg, 2014, pp. 229–266, https://doi.org/10.1007/978-3-642-53980-0_8.
[48] K. Tõnsuaadu, K.A. Gross, L. Plūduma, M. Veiderma, A review on the thermal stability of calcium apatites, J. Therm. Anal. Calorim. 110 (2012) 647–659, https://doi.org/10.1007/s10973-011-1877-y.
[49] S. Ramesh, K.L. Aw, R. Tolouei, M. Amiriyan, C.Y. Tan, M. Hamdi, J. Purbolaksono, M.A. Hassan, W.D. Teng, Sintering properties of hydroxyapatite powders prepared using different methods, Ceram. Int. 39 (2013) 111–119, https://doi.org/10.1016/j.ceramint.2012.05.103.
[50] M. Prakasam, J. Locs, K. Salma-Ancane, D. Loca, A. Largeteau, L. Berzina-Cimdina, Fabrication, properties and applications of dense hydroxyapatite: a review, J. Funct. Biomater. 6 (2015) 1099–1140, https://doi.org/10.3390/jfb6041099.
[51] J.G. Fernandes, Development and Optimization of a Low Temperature Co-fired Ceramic Suspension for Mask-Image-Projection-Based Stereolithography, Ph.D. Thesis, Universitat de Barcelona, 2019, http://www.tdx.cat/handle/10803/667478.
[52] A. Farzadi, M. Solati-Hashjin, M. Asadi-Eydivand, N.A.A. Osman, Effect of layer thickness and printing orientation on mechanical properties and dimensional accuracy of 3D printed porous samples for bone tissue engineering, PLoS One 9 (2014), e108252, https://doi.org/10.1371/journal.pone.0108252.
[53] T.-R. Kim, M.-S. Kim, T.S. Goh, J.S. Lee, Y.H. Kim, S.-Y. Yoon, C.-S. Lee, Evaluation of structural and mechanical properties of porous artificial bone scaffolds fabricated via advanced TBA-based freeze-gel casting technique, Appl. Sci. 9 (2019) 1965, https://doi.org/10.3390/app9091965.
[54] V. Karageorgiou, D. Kaplan, Porosity of 3D biomaterial scaffolds and osteogenesis, Biomaterials 26 (2005) 5474–5491, https://doi.org/10.1016/j.biomaterials.2005.02.002.
[55] M. Houmard, Q. Fu, M. Genet, E. Saiz, A.P. Tomsia, On the structural, mechanical, and biodegradation properties of HA/β-TCP robocast scaffolds, J. Biomed. Mater. Res. 101 (2013) 9, https://doi.org/10.1002/jbm.b.32935.
[56] C.S. Lee, S.G. Kim, H.J. Kim, S.H. Ahn, Measurement of anisotropic compressive strength of rapid prototyping parts, J. Mater. Process. Technol. 187–188 (2007) 627–630, https://doi.org/10.1016/j.jmatprotec.2006.11.095.
[57] J. Saini, L. Dowling, J. Kennedy, D. Trimble, Investigations of the mechanical properties on different print orientations in SLA 3D printed resin, Proc. IME C J. Mech. Eng. Sci. 234 (2020) 2279–2293, https://doi.org/10.1177/0954406220904106.
[58] I. Sabree, J.E. Gough, B. Derby, Mechanical properties of porous ceramic scaffolds: influence of internal dimensions, Ceram. Int. 41 (2015) 8425–8432, https://doi.org/10.1016/j.ceramint.2015.03.044.
[59] B. Basu, Mechanical properties of biomaterials, in: Biomaterials for Musculoskeletal Regeneration, Springer Singapore, Singapore, 2017, pp. 175–222, https://doi.org/10.1007/978-981-10-3059-8_6.
[60] P.N. Sudha, S. Kirubanandam, J. Av, V. N, R. Kannan, Corrosion of ceramic materials, in: Fundamental Biomaterials: Ceramics, 2018, pp. 223–250, https://doi.org/10.1016/B978-0-08-102203-0.00009-3.
[61] M. Fulmer, I. Ison, C. Hankermayer, B. Constantz, J. Ross, Measurements of the solubilities and dissolution rates of several hydroxyapatites, Biomaterials 23 (2002) 751–755, https://doi.org/10.1016/S0142-9612(01)00180-6.
[62] N. Eliaz, N. Metoki, Calcium phosphate bioceramics: a review of their history, structure, properties, coating technologies and biomedical applications, Materials 10 (2017) 334, https://doi.org/10.3390/ma10040334.
[63] S. Vahabzadeh, M. Roy, A. Bandyopadhyay, S. Bose, Phase stability and biological property evaluation of plasma sprayed hydroxyapatite coatings for orthopedic and dental applications, Acta Biomater. 17 (2015) 47–55, https://doi.org/10.1016/j.actbio.2015.01.022.
[64] S.V. Dorozhkin, M. Epple, Biological and medical significance of calcium phosphates, Angew Chem. Int. Ed. Engl. 41 (2002) 3130–3146, https://doi.org/10.1002/1521-3773(20020902)41:17<3130::AID-ANIE3130>3.0.CO;2-1.